Supporting Information

Trapping $[PMo_{12}O_{40}]^{3-}$ clusters into pre-synthesized ZIF-67 toward Mo_XCo_XC particles Confined in Uniform Carbon Polyhedron for Efficient Overall Water Splitting

Congfang Chen, Aiping Wu, Haijing Yan, Yinglu Xiao, Chungui Tian* and Honggang Fu*

The content of ESI

1. Experimental Section.
2. The content calculated based on ICP.
3. Table S1. The samples and their corresponding synthesis parameters.
4. Figure S1. SEM image of S-PMo/ZIF-67.
5. Figure S2. (a) UV-vis spectra of $Co(NO_3)_2 \cdot 6H_2O$ and (b) 2-MIM in methanol with differrent concentration. (c) UV-vis spectra of the supernatant separated from (A) hot and (B) cooling dispersion from treating methanol solution of ZIF-67 at 100 °C for 6h in water bath condition. (d) UV-vis spectra of PMo_{12} in 60ml methanol and the supernatant separated from dispersion of PMo/ZIF-67-2, PMo/ZIF-67-6 and PMo/ZIF-67-10.
6. Figure S3. (a) XPS survey spectra and high-resolution spectra of (b) Mo 3d of PMo/ZIF-67-6.
7. Figure S4. SEM image of ZIF-67.
8. Figure S5. XRD patterns of PMo/ZIF-67-6-6N.
9. Figure S6. XRD patterns of PMo/ZIF-67-6-6N taken on X-ray powder diffractometer with high power (6 KW).
10. Figure S7. SEM image of ZIF-67-6N.
11. Figure S8. EDS mapping of N and P for PMo/ZIF-67-6-6N. Scale bar is 500 nm
12. Figure S9. TG curve of PMo_{12}/ZIF-67-6-6N tested in air atmosphere.
13. Figure S10. High-resolution scans of N 1s and P 2p of PMo/ZIF-67-6-6N (M

represented Mo or Co).

14. Figure S11. XRD patterns of PMo/ZIF-67-6-6N after etching away of Co with IM H_2SO_4.

15. Figure S12. (a) EDX spectrum, (b) STEM image and corresponding to EDS mapping of Mo, Co, C, N and P for PMo/ZIF-67-6-6N-E (The E presents the etching away of Co NPs in H_2SO_4)

16. Figure S13. (a) XPS survey spectra and high-resolution spectra of (b) Co 2p, c) Mo 3d, of PMo/ZIF-67-6-6N after etching with H_2SO_4 (PMo/ZIF-67-6-6N-E).

17. Figure S14. (a) XRD patterns of PMo/ZIF-67-6-5N, PMo/ZIF-67-6-7N, PMo/ZIF-67-6-8N and ZIF-67-7N; (b) the SEM image of PMo/ZIF-67-6-7N.

18. Figure S15. SEM images of (a) PMo/ZIF-67-2, (b) PMo/ZIF-67-6 and (c) PMo/ZIF-67-10. The TEM images of (d) PMo/ZIF-67-2, (e) PMo/ZIF-67-6 and (f) PMo/ZIF-67-10. The g-j is TG curves of PMo/ZIF-67-2, PMo/ZIF-67-6 and PMo/ZIF-67-10 under air atmosphere.

19. Figure S16. SEM image of Na_2MoO_4/ZIF-67-6 prepared with Na_2MoO_4 as Mo source.

20. Figure S17. XRD patterns of PMo/ZIF-67-6-7N and Na_2MoO_4/ZIF-67-6-7N prepared in the presence of $H_3PMo_{12}O_{40}$ and $Na_2MoO_4 \cdot 2H_2O$ as Mo source, respectively.

21. Scheme S1. The formation mechanism of PMo/ZIF-67.

22. Figure S18. Cyclic voltammograms (CV) of PMo/ZIF-67-6-6N (a) and ZIF-67-6N (c) taken under different rates from 40 to 220 mVs^{-1}. The corresponding capacitive current at 0.15 V as a function of scan rate for PMo/ZIF-67-6-6N (b) and ZIF-67-6N (d).

23. Figure S19. (a) Polarization curves of the PMo/ZIF-67-6 calcinated at 500, 600, 700 and 800℃under N_2 in 1M KOH at the scan rate of 5 mVs^{-1} for HER. (b) Polarization curves of PMo/ZIF-67-2-6N, PMo/ZIF-67-6-6N and PMo/ZIF-67-10-6N in 1M KOH at the scan rate of 5 mVs^{-1} for HER. (c) Polarization curves of Na_2MoO_4/ZIF-67-6-6N and PMo/ZIF-67-6-6N under the same condition for HER.

24. Figure S20. N_2 adsorption-desorption isotherms of PMo/ZIF-67-6-6N.

25. Figure S21. Work function (WF) drawings of (a) PMo/ZIF-67-6-6N , (b) Pt/C and (c) ZIF-67-6N.

26. Figure S22. (a) Polarization curves of PMo/ZIF-67-6 calcinated at 500, 600, 700 and 800℃under N_2 in 1M KOH at the scan rate of 5 mVs^{-1} for OER. (b) Polarization curves of PMo/ZIF-67-2-7N, PMo/ZIF-67-6-7N and PMo/ZIF-67-10-7N in 1M KOH at the scan rate of 5 mVs^{-1} for OER. (c) Polarization curves of Na_2MoO_4/ZIF-67-6-7N and PMo/ZIF-67-6-7N under the same condition for OER.

27. Figure S23. Cyclic voltammograms (CV) of (a) PMo/ZIF-67-6-7N and (c) ZIF-67-7N taken under different rates from 40 to 220 mVs-1. The corresponding capacitive currents at 1.25 V as a function of scan rate for (b) PMo/ZIF-67-6-7N and (d) ZIF-67-7N.

28. Figure S24. The experimentally determined and theoretically calculated amounts of H_2 on PMo/ZIF-67-6-6N and O_2 on PMo/ZIF-67-6-7N.

29. Figure S25. HER performance of PMo/ZIF-67-6-6N and PMo/ZIF-67-6-6N-E (E represented etching) in 1M KOH. The performance have no obvious change before and after etching of Co NPs.

30. Figure S26. XRD pattern of PMo/ZIF-67-6-7N after OER test (40 CV cycles).

31. Figure S27. XPS of Co2p of PMo/ZIF-67-6-7N after OER test (40 CV cycles).

32. Figure S28. XPS of Mo3d of PMo/ZIF-67-6-7N after OER test (40 CV cycles).

33. Figure S29. The OER performance of PMo/ZIF-67-6-7N and PMo/ZIF-67-6-7N-E (E represented etching of Co NPs in H_2SO_4) in 1M KOH. The η_{10} and η_{100} for PMo/ZIF-67-6-7N are 295 and 370mV respectively, lower than 320 and 410mV for PMo/ZIF-67-6-7N-E. The result indicate the contribution of Co NPs in PMo/ZIF-67-6-7N on OER.

34. Figure S30. The photograph for overall water splitting reaction in a two-electrode configuration. The inset is an optical photograph showing the generation of H_2 and O_2 bubbles for PMo/ZIF-67-6-6N||PMo/ZIF-67-6-7N on Ni foam.

35. Figure S31. SEM image of S-PMo/ZIF-67-6N.

36. Figure S32. XRD patterns of S-PMo/ZIF-67-6N.

37. Figure S33. Polarization curves of PMo/ZIF-67-6-6N and S-PMo/ZIF-67-6N in

1M KOH at the scan rate of 5 mVs^{-1} for HER.

38. Figure S34. Polarization curves of PMo/ZIF-67-6-7N and S-PMo/ZIF-67-6N in 1M KOH at the scan rate of 5 mVs^{-1} for OER.

39. Table S2. Comparison of HER performance of PMo/ZIF-67-6-6N with other non-noble metal HER electrocatalysts in alkaline conditions.

40. Table S3. The HER performance of catalysts from the calcination of PMo/ZIF-67-6 at different temperature.

41. Table S4. The HER performance of catalysts prepared by the calcination of PMo/ZIF-67 from different solvothermal time.

42. Table S5. The HER performance of catalysts from the calcination of the precursor prepared by using Na_2MoO_4 and PMo_{12} as Mo source.

43. Table S6. The HER performance of catalysts prepared based on “tapping” route and “simultaneous” route (POMOF-based route).

44. Table S7. The OER performance of catalysts from the calcination of PMo/ZIF-67-6 at different temperature.

45. Table S8. The OER performance of catalysts prepared by the calcination of PMo/ZIF-67 from different solvothermal time.

46. Table S9. The OER performance of catalysts from the calcination of the precursor prepared by using Na_2MoO_4 and PMo_{12} as Mo source.

47. Table S10. The OER performance of catalysts prepared based on “tapping” route and “simultaneous” route (POMOF-based route).

48. Table S11. Comparison of OER performance of PMo/ZIF-67-6-7N with other non-noble metal OER electrocatalysts in alkaline conditions.

49. Table S12. The performance of the recent reported electrocatalysts in alkaline solution for overall water splitting.

1. Experimental Section

The synthesis procedure of other control samples

The experimental parameters, including the solvothermal time, the amount of PMo_{12} and the kind of Mo source, were tuned to regulate the micro-structure of final materials. The solids obtained after solvothermal reaction at 100℃ for 2 h and 10h were denoted as PMo/ZIF-67-2 and PMo/ZIF-67-10. The PMo/ZIF-67-6 (0.066), PMo/ZIF-67-6 (0.165) and PMo/ZIF-67-6 (0.660) were also prepared under the same condition with PMo/ZIF-67-6, excepting the use of 0.066, 0.165 and 0.660 mmol of PMo12 instead of 0.330 mmol of PMo_{12}. The Na_2MoO_4/ZIF-67-6 was obtained by using Na_2MoO4 as Mo source instead of PMo_{12}. Unless otherwise specified, the PMo/ZIF-67-X represents the samples which was prepared by solvothermal treatment of ZIF-67 in the presence of 0.330 mmol PMo_{12}.

Synthesis of S-PMo/ZIF-67

S-PMo/ZIF-67 was synthesized through the simultaneous addition of POMs, 2-MIM and Co^{2+} salts in solution (a route similar to that used for the synthesis of POMOF). After reaction at room temperature for 6h, the solid was separated by filtration, and was washed with methanol for three times. And then the solid was dried at 60 °C in a vacuum oven for 12 h. (S in S-PMo/ZIF-67 represented “simultaneous”)

Synthesis of S-PMo/ZIF-67-6N

The procedure was similar to the synthesis of PMo/ZIF-67-6-6N excepting the replacement of PMo/ZIF-67-6 with S-PMo/ZIF-67.

2. The content calculated based on ICP

(1) The ICP test indicated the amount of Mo in PMo/ZIF-67-6 is about 21.5%. So, the amount of PMo_{12} in PMo/ZIF-67-6 can be calculated as follows (MW is Molecular weight):

$PMo_{12}\%$ = Mo% ×MW of PMo_{12}/12 MW of Mo = 21.5% ×1825.25/1151.52=34.1%

(2) We have analyzed Co content from Co NPs in PMo/ZIF-67-67-6N based on ICP analysis. For this test, the PMo/ZIF-67-67-6N was firstly treated by inaqua regia to solve Co and Mo components. The solution was set the certain volume with deionized water, and the total concentration of Co ($Co_{(T)}$) and Mo ($Mo_{(T)}$) ions in solution were analyzed by ICP analyser. The amount of Co ions from Co_6Mo_6C (Co in Co_6Mo_6C) is calculated based on the followed formula:

$$\text{Content (Co) in } Co_6Mo_6C = Mo_{(T)} \times 58.93/95.94 = 0.614Mo_{(T)}$$

The content of Co from Co NPs can be calculated by deducting Co in Co_6Mo_6C from $Co_{(T)}$. The Co mass from Co NPs is about 26% based above analyses.

Table S1. The samples and their corresponding synthesis parameters.

Entry	Samples	Solvothermal (trapping) Time (h)	Calcination temperature (°C)	Calcination Time (h)	n (Mo source) (mmol)
1	ZIF-67-6N	0	600	4	0 ($H_3PMo_{12}O_{40}$)
2	ZIF-67-7N	0	700	4	0 ($H_3PMo_{12}O_{40}$)
3	PMo/ZIF-67-6-5N	6	500	4	0.330 ($H_3PMo_{12}O_{40}$)
4	PMo/ZIF-67-6-6N	6	600	4	0.330 ($H_3PMo_{12}O_{40}$)
5	PMo/ZIF-67-6-7N	6	700	4	0.330 ($H_3PMo_{12}O_{40}$)
6	PMo/ZIF-67-6-8N	6	800	4	0.330 ($H_3PMo_{12}O_{40}$)
7	PMo/ZIF-67-2-6N	2	600	4	0.330 ($H_3PMo_{12}O_{40}$)
8	PMo/ZIF-67-10-6N	10	600	4	0.330 ($H_3PMo_{12}O_{40}$)
9	PMo/ZIF-67-2-7N	2	700	4	0.330 ($H_3PMo_{12}O_{40}$)
10	PMo/ZIF-67-10-7N	10	700	4	0.330 ($H_3PMo_{12}O_{40}$)
11	PMo/ZIF-67-6-6N (0.066)	6	600	4	0.066 ($H_3PMo_{12}O_{40}$)
12	PMo/ZIF-67-6-6N (0.165)	6	600	4	0.165 ($H_3PMo_{12}O_{40}$)
13	PMo/ZIF-67-6-6N (0.660)	6	600	4	0.660 ($H_3PMo_{12}O_{40}$)
14	PMo/ZIF-67-6-7N (0.066)	6	700	4	0.066 ($H_3PMo_{12}O_{40}$)
15	PMo/ZIF-67-6-7N (0.165)	6	700	4	0.165 ($H_3PMo_{12}O_{40}$)
16	PMo/ZIF-67-6-7N (0.660)	6	700	4	0.660 ($H_3PMo_{12}O_{40}$)
17	Na_2MoO_4/ZIF-67-6-6N	6	600	4	3.960 ($Na_2MoO_4 \cdot 2H_2O$)
18	Na_2MoO_4/ZIF-67-6-7N	6	700	4	3.960 ($Na_2MoO_4 \cdot 2H_2O$)

*** In all syntheses, the amount of ZIF-67 is 0.452 mmol (0.1g). The total volume of methanol solvent is 60 mL.**

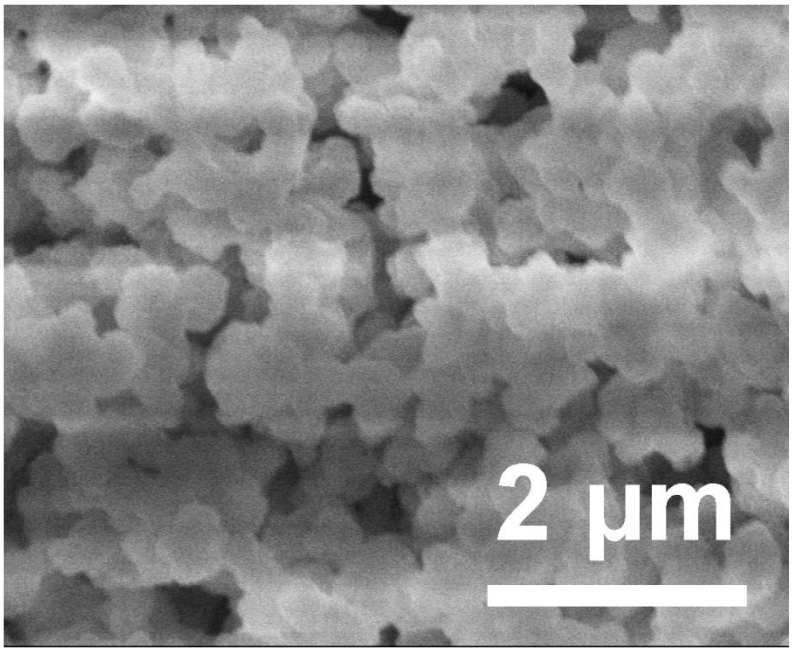

Figure S1. SEM image of S-PMo/ZIF-67.

Figure S1 shows SEM image of S-PMo/ZIF-67 from the simultaneous addition of POMs, 2-MIM and Co^{2+} salts in solution (a route similar to POMOF). It can be obviously seen the presence of un-uniform sphere, which is obviously different from the regular polyhedron morphology of PMo/ZIF-67 from "trapping" route. The results indicate the less controllability of the "direct" route on the structure due to difficult in coordinating the reaction rate both of Co^{2+} and PMo_{12} with 2-MIM.

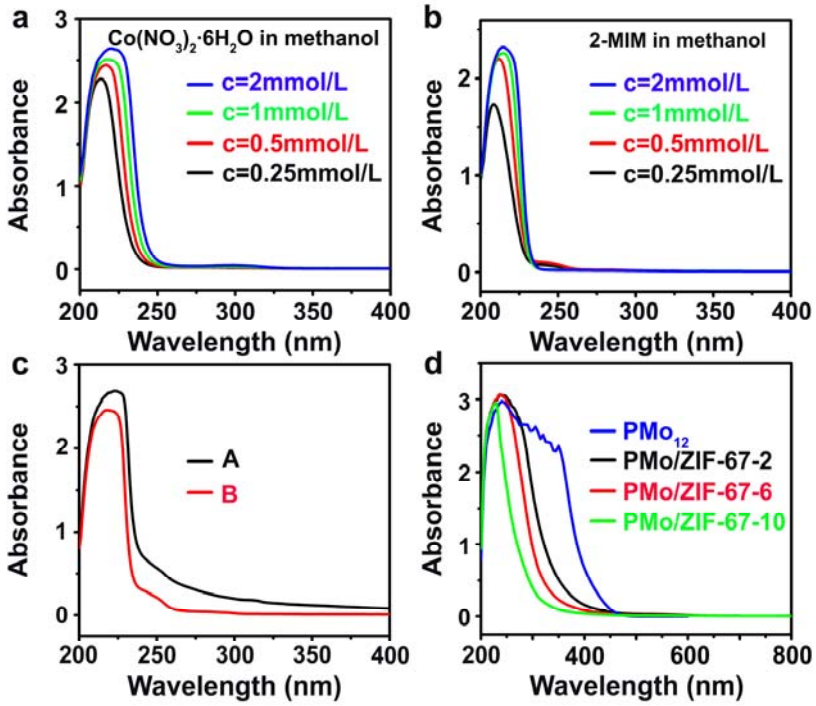

Figure S2. (a) UV-vis spectra of $Co(NO_3)_2 \cdot 6H_2O$ and (b) 2-MIM in methanol with

differrent concentration. (c) UV-vis spectra of the supernatant separated from (A) hot and (B) cooling dispersion from treating methanol solution of ZIF-67 at 100 ^{o}C for 6h in water bath condition. (d) UV-vis spectra of PMo_{12} in 60mL methanol and the supernatant separated from dispersion of PMo/ZIF-67-2, PMo/ZIF-67-6 and PMo/ZIF-67-10.

The ZIF-67 have large cage with size of 1.16 nm. The size of PMo_{12} is about 1 nm. So, in principle, the cage of ZIF-67 can accommodate PMo_{12} with the fashion of one PMo_{12} in one cage. However, the window aperture of ZIF-67 is too small (0.34 nm) to allow the access of PMo_{12} into pre-synthesized ZIF-67. Opening the window will provide the large avenue to allow the assess of PMo_{12} into the cage. It is known that there is the presence of the precipitation-dissolution equilibrium in the dispersion of the solid. For MOF solid, the process should also exist, and is called as disassembly-reassembly equilibrium. The disassembly process will result in the presence of dissociative Co^{2+} and 2-MIM in solution. Based on UV-vis test, we have found that the methanol solution of $Co(NO_3)_2$ and 2-MIM have shown obvious adsorption peaks in the range of 200-250 nm (Figure S2a, b). The adsorption intensity increases with the increase of concentration of both Co^{2+} and 2-MIM, although it have not linear relation between the concentration and adsorption. So, we have studied the degree of disassembly based on UV-vis methods. To this, the dispersion liquid of ZIF-67 (0.452 mmol) in methanol (60 mL) was heated in water bath (100^{o}C) for 6h. After heating, the dispersion liquid of ZIF-67 in methanol was treated by two different ways.

In the first way, the dispersion liquid was cooled to room temperature, and then centrifuged to separate solid and solution. Figure S2c shows UV-vis spectra of supernatant. We can see the obvious absorbance at ～220nm. The absorbance should be from Co ions and 2-MIM disassembly from ZIF-67. The total concentration is about 0.5 mmol L^{-1} by comparing with UV-vis spectra of Co^{2+} (Figure S2a) and 2-MIM (Figure S2b) solution. Assuming all Co^{2+} and 2-MIM are disassemblied from 0.452 mmol of ZIF-67 (0.1g) in 60mL methanol, the concentration of Co^{2+} and

2-MIM is about 7.53 mmol L^{-1} and 15.06 mmol L^{-1}. UV-vis spectra test indicates that a part of Co^{2+} and 2-MIM disassembled from ZIF-67. The removal of a number of linkers or metal nodes can not cause collapse of the framework structure due to the high degree of connectivity of MOF[1]. The loss of ligand or metal ions can result in the formation of large avenue in MOF (UIO-66), facilitating the developement of catalytic activity[2], adsorbance of water molecular[3] and accommodation of guest molecular[4]. In our work, the disassembly process can also make the formation of some defect, thus opening the window of ZIF-67 and allowing the access of PMo_{12} into ZIF-67 cage.

In the second way , the solid was separated fast and directly from hot reaction solution after reaction. The supernatant have shown stronger absorbance at ～220nm than that separated from cooling dispersion, implying the high concentration of Co^{2+} and 2-MIM in hot solution (Figure S2c). The trapping process was performed at higher temperature (100^{o}C under solvothermal condition), which can result in the release of more Co^{2+} and 2-MIM from ZIF-67 (more defect). The test implies the reassembly of a part of Co^{2+} and 2-MIM on ZIF-67 under cooling process, which facilitate the encapsulation of guest molecular.

Based on above analysis, the trapping of PMo_{12} into ZIF-67 can be proposed as follows: there are presence of dynamic diassembly-reassembly process after dispersion of ZIF-67 into methanol under heating. Some Co^{2+} and 2-MIM can be released from ZIF-67 to solution. The process can make the “opening” of the window of ZIF-67, thus creating the large avenue. The cage can accommodate PMo_{12} after opening the window due to the suitable size (1.16nm vs 1.0 nm). Also, the residual 2-MIM in cage can coordinate with PMo_{12}, making the stabilization of PMo_{12} in cage. The reassembly of Co^{2+} and 2-MIM on ZIF-67 (especially under cooling process) and the coordination between PMo_{12} with residual 2-MIM in cage can make the stabilization and encapsulation of PMo_{12} in cage.

Figure S2d shows the UV-vis spectra of PMo_{12} in 60mL methanol and the supernatant separated from dispersion of PMo/ZIF-67-2, PMo/ZIF-67-6 and

PMo/ZIF-67-10. We can see that peaks of PMo_{12} in solution gradually decrease with prolonging the solvothermal time, implying its trapping in ZIF-67. The intensive adsorption peaks in Figure S2d indicated that more Co^{2+} and 2-MIM were deassembled from ZIF-67 under solvothermal condition at 100°C, being favorable for more effective trapping of PMo_{12} into ZIF-67.

[1] L. Valenzano, B. Civalleri, S. Chavan, S. Bordiga, M.H. Nilsen, S. Jakobsen, K.P. Lillerud, C. Lamberti, Chem. Mater., 2011, 23, 1700-1718.

[2] S. M. J. Rogge, A. Bavykina, J. Hajek, H. Garcia, A. I. Olivos-Suarez, S. M. J. Rogge, A. Bavykina, J. Hajek, H. Garcia, A. I. Olivos-Suarez, A. Sepúlveda-Escribano, A. Vimont, G. Clet, P. Bazin, F. Kapteijn, M. Daturi, E. V. Ramos-Fernandez, F. X. Llabrés Xamena, V. Van Speybroeck and J. Gascon, Chem. Soc. Rev., 2017, 46, 3134-3184.

[3] Pritha Ghosh, Yamil J. Colón and Randall Q. Snurr, Chem. Commun., 2014, 50, 11329-11331.

[4] Marco Taddei, Coordination Chemistry Reviews, 2017, 343, 1-24.

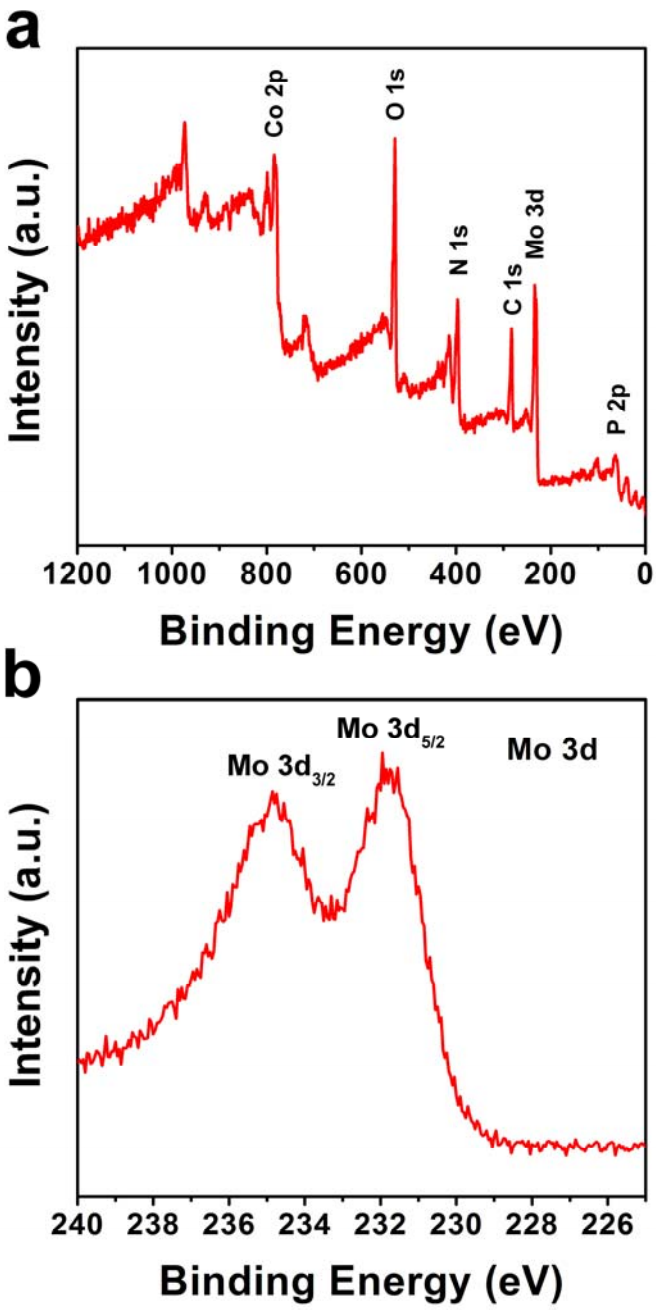

Figure S3. (a) XPS survey spectra and high-resolution spectra of (b) Mo 3d of PMo/ZIF-67-6.

The XPS survey spectrum shows the presence of Co, Mo, C, N, O, P in PMo/ZIF-67-6, implying a combination of PMo_{12} and ZIF-67. In the high-resolution spectrum of Mo 3d of PMo/ZIF-67-6, there are two peaks. The peak at 231.8 eV and 234.8eV are related to $3d_{5/2}$ and $3d_{3/2}$, respectively. The peaks have shifted to lower energy region in comparison with PMo_{12}, which should be relative with the partial electronic interaction of PMo_{12} clusters with ZIF-67 host.

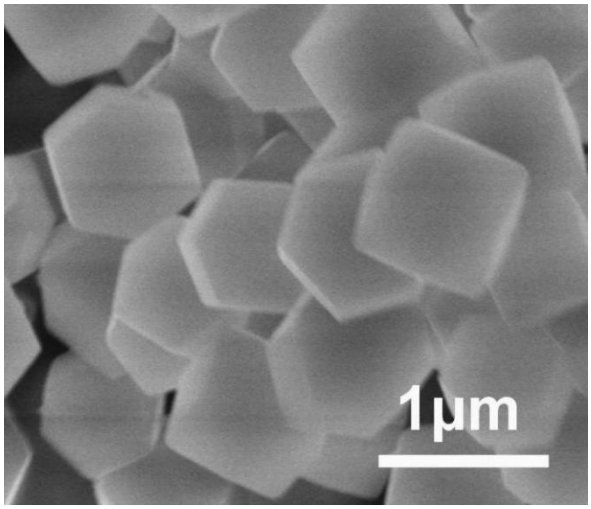

Figure S4. SEM image of ZIF-67.

Figure S4 shows SEM image of ZIF-67. It can be clearly observed that the formation of ZIF-67 with polyhedron morphology and uniform size.

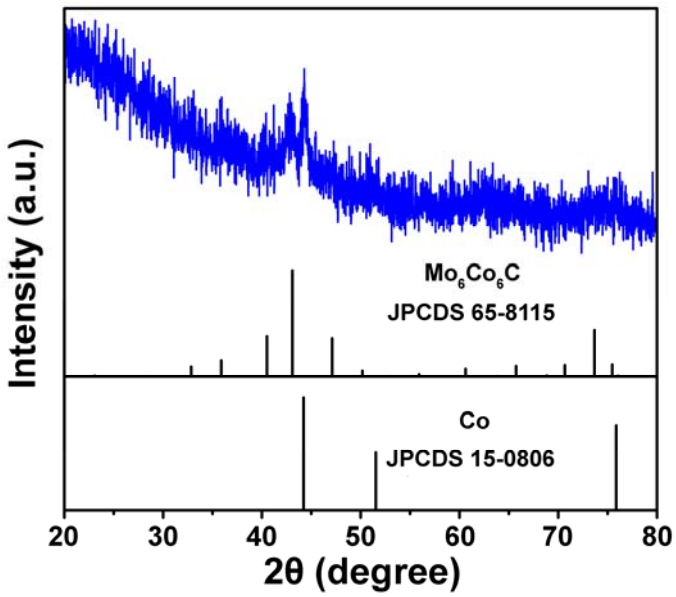

Figure S5. XRD patterns of PMo/ZIF-67-6-6N.

Figure S5 shows XRD patterns of PMo/ZIF-67-6-6N. The peaks located at 32.83, 35.88, 40.50, 53.08, 47.12, 70.67, 73.67, and 75.45 can be observed, which indexed to (400), (331), (422), (511), (440), (733), (822), and (555) planes of Mo_6Co_6C, respectively (JPCDS 65-8115). The peaks located at 44.2, 51.5 and 75.8 correspond to (111), (200) and (220) planes of Co (JPCDS 15-0806). The test indicates the formation of Mo_6Co_6C after calcinating PMo/ZIF-67-6 under N_2.

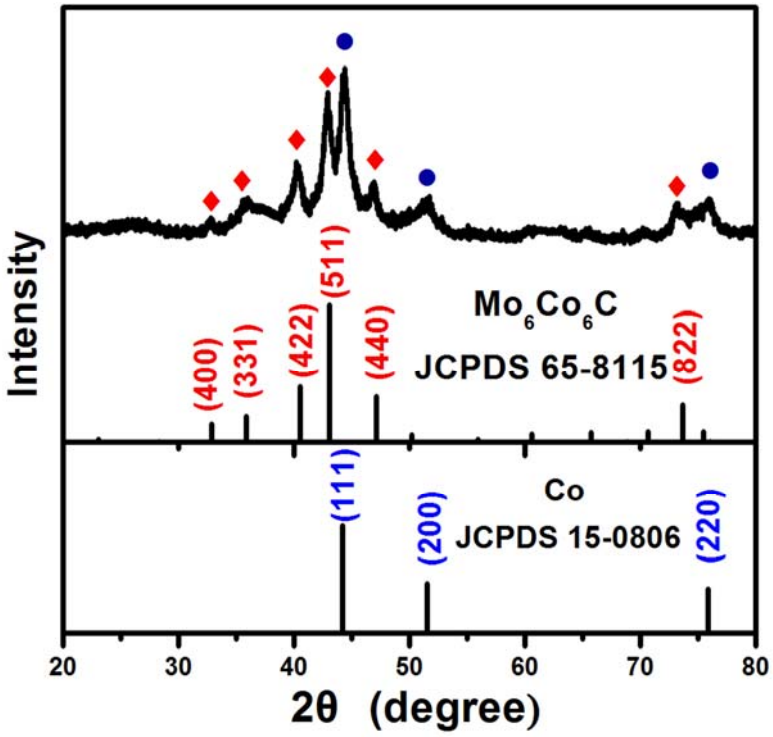

Figure S6. XRD patterns of PMo/ZIF-67-6-6N taken on X-ray powder diffractometer with high power (6 KW).

To solidly prove the existence of Co_6Mo_6C, we have performed the XRD test on X-ray powder diffractometer with high power (6 KW). We can see the obvious diffraction peaks of Co_6Mo_6C in the pattern. The peaks located at 2θ = 43.1°, 40.5°, 35.8°, 32.8° and 47.2° and 73.7° can be indexed to (511), (422), (331), (400), (440) and (822) planes of Co_6Mo_6C. The peaks located at 2θ= 44.2°, 51.5°, 75.8° should be indexed to (111), (200), (220) planes of metal Co.

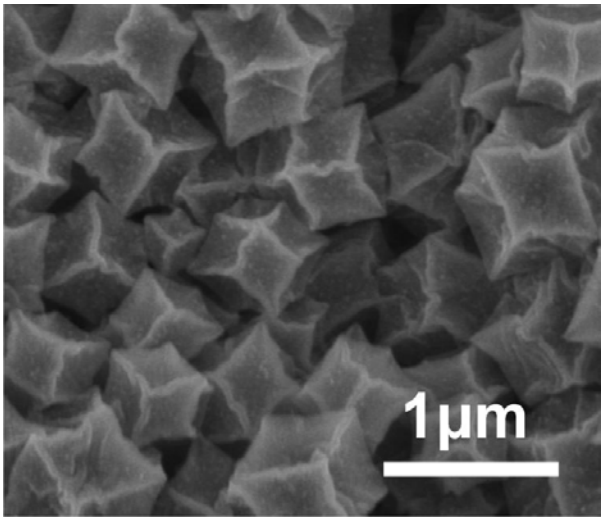

Figure S7. SEM image of ZIF-67-6N.

Figure S7 shows SEM image of ZIF-67-6N. We can see the presence of polyhedron with uniform size. Being different from ZIF-67, the surface of polyhedron in ZIF-67-6N was very rough, implying the formation of nanoparticles.

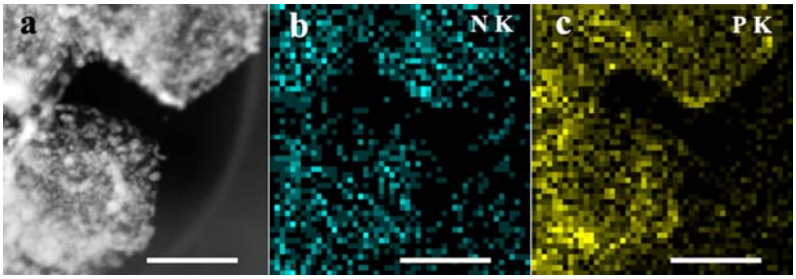

Figure S8. EDS mapping of N and P for PMo/ZIF-67-6-6N. Scale bar is 500 nm.

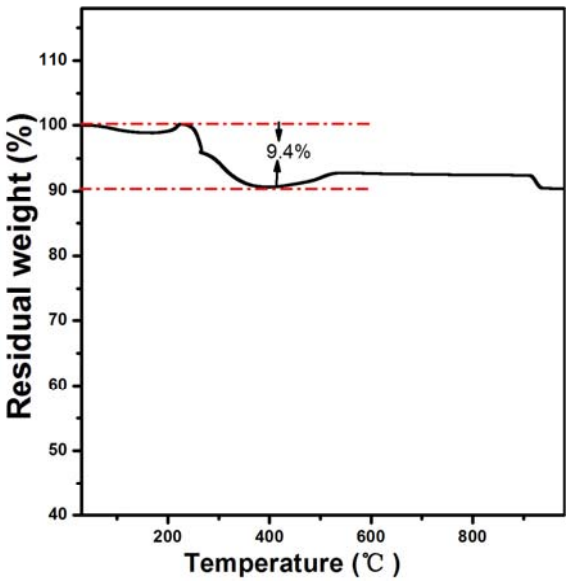

Figure S9. TG curve of PMo_{12}/ZIF-67-6-6N tested in air atmosphere.

Figure S9 shows TG curve of PMo_{12}/ZIF-67-6-6N. A obvious loss weight between room temperature and 400^{o}C should be ascribed to the decomposition of carbon. The increase of weight between 530 to 900^{o}C should be due to the oxidation of Mo and Co species. The amount of carbon in PMo_{12}/ZIF-67-6-6N is about 9.4% based on TG analysis.

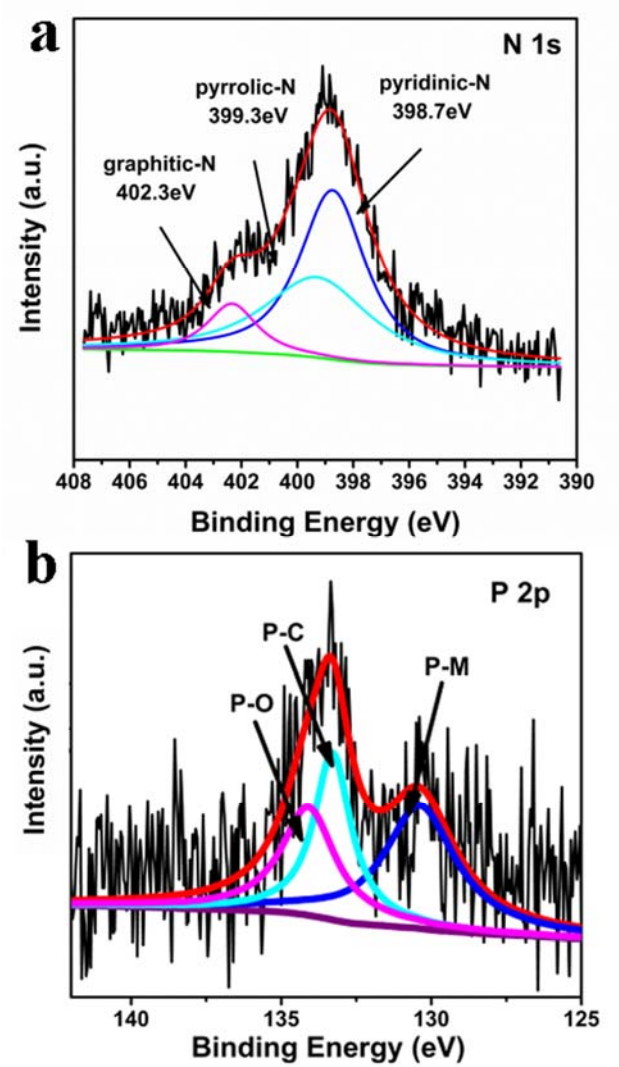

Figure S10. High-resolution scans of N 1s and P 2p of PMo/ZIF-67-6-6N (M represented Mo or Co)

The high-resolution of N 1s XPS peaks can be divided into three peaks, the peaks at 397.8 eV, 399.3 eV and 399.2 eV denotes to the pyridinic-N, pyrrolic-N and graphitic-N respectively. Compared with the pyrrolic-N, Pyridinic-N and graphitic-N exhibit higher activity ,which is conducive to enhancing catalytic activity. After deconvolution of curve, we can see the sub-peaks associated with P-O (13.4.2 eV), P-C (133.2 eV). The peaks at 130.4 eV should be ascribed to P-Mo or P-Co. Based on PMo_{12} structure, the P is surround by Mo, thus it can easily combine with Mo in the products due to close distance of Mo and P.

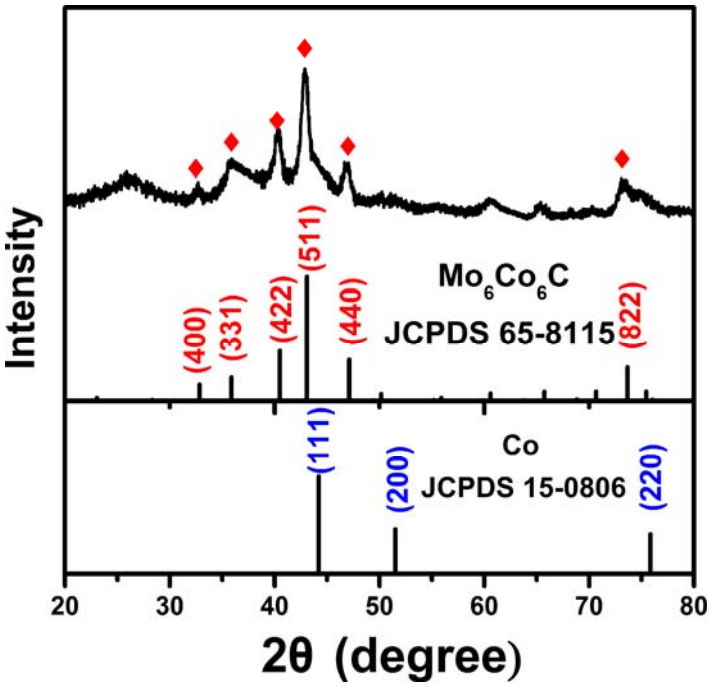

Figure S11. XRD patterns of PMo/ZIF-67-6-6N after etching away of Co with IM H_2SO_4.

After etching in 1M H_2SO_4, most of Co can be removed and Co_6Mo_6C@Carbon can be obtained.The peaks located at 2θ = 43.1°, 40.5°, 35.8°, 32.8° and 47.2° and 73.7° can be indexed to (511), (422), (331), (400), (440) and (822) planes of Co_6Mo_6C. No obvious peaks about metal Co can be observed.

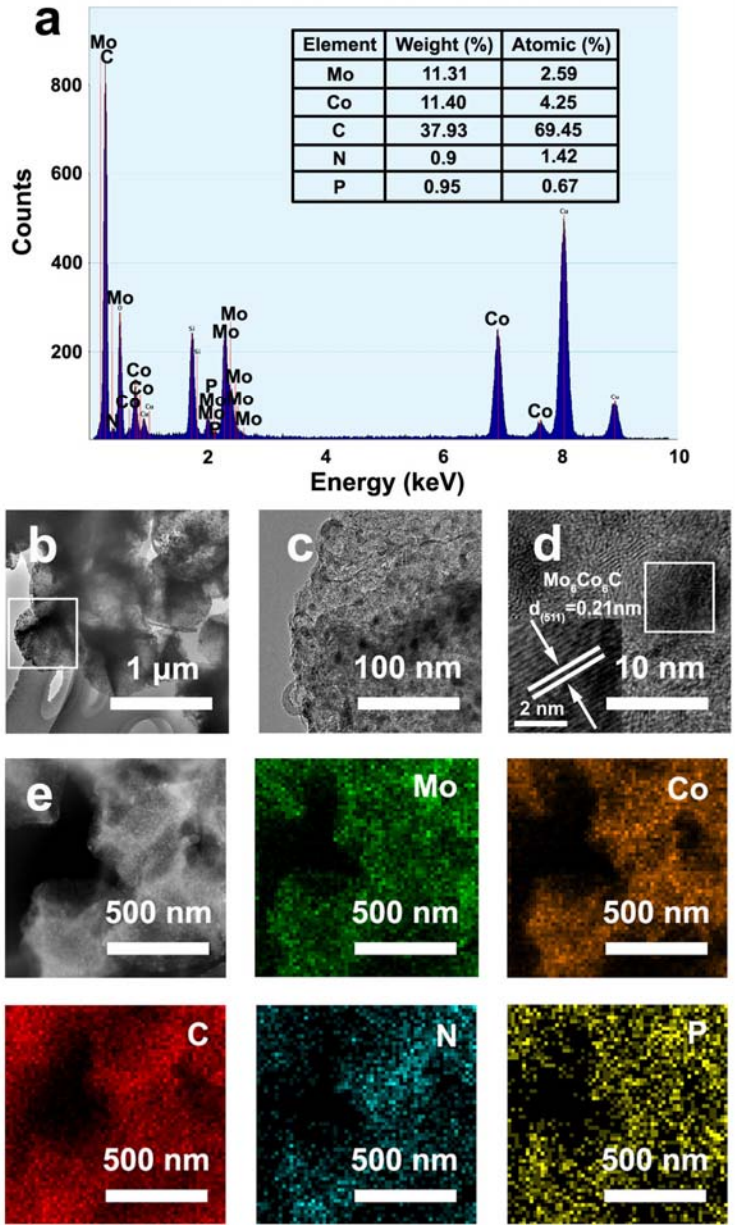

Figure S12. (a) EDX spectrum, (b-d) TEM, (e) STEM image and corresponding to EDS mapping of Mo, Co, C, N and P for PMo/ZIF-67-6-6N-E (The E presents the etching away of Co NPs in H_2SO_4).

EDX spectrum shows that the ratio of Co/Mo from TEM-EDX is about 1.64. TEM test of Co_6Mo6C@C shows the uniform distribution of small particles encapsulated in carbon polyhedrons, being similar with that of PMo/ZIF-67-6-6N. The HRTEM of one particles shows the interplanar distance of 0.21 nm, which is indexed to (511) plane of Mo_6Co_6C. The EDS mapping confirms the uniform distribution of Co, Mo, C, P, N (Figure S8) through the polyhedrons.

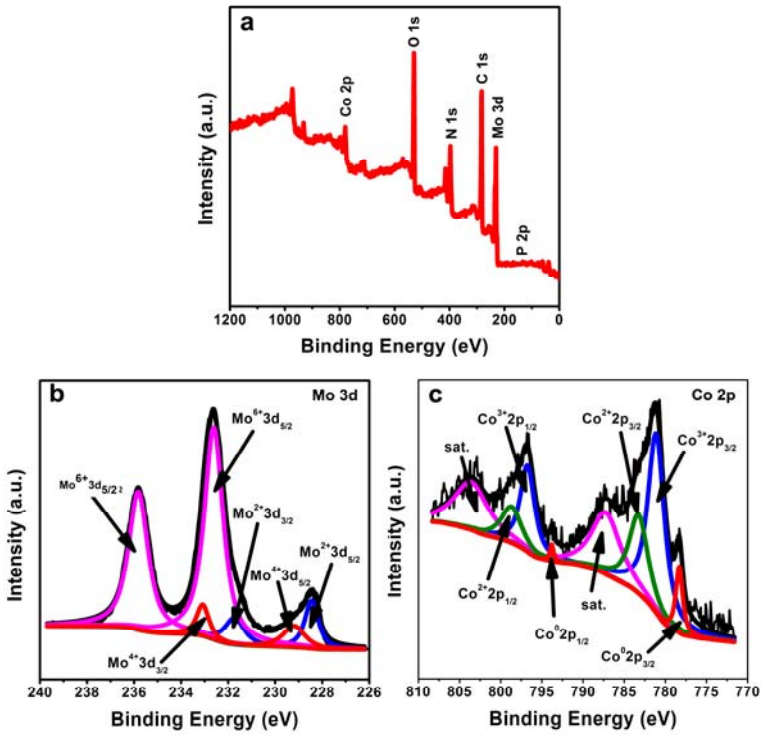

Figure S13. (a) XPS survey spectra and high-resolution spectra of (b) Co 2p, (c) Mo 3d, of PMo/ZIF-67-6-6N after etching with H_2SO_4 (PMo/ZIF-67-6-6N-E).

After removing Co NPs, the XPS spectra of Co2p and Mo3d are consistent with that in Mo_6Co_6C. For Mo3d, a sub-peak corresponding to Mo^{4+} can be observed after deconvolution of curve, which should be due to slight oxidation of Mo species in etching process by H_2SO_4 (Figure S13b). In Co2p XPS, the sub-peaks indexed to Co^{2+}, Co^{3+} and Co^0 can be observed. The presence of Co^0 shows the presence of Co NPs still after etching due to protecting role of carbon layers. However, the ratio of Co^0 for PMo/ZIF-67-6-6N-E has much lower than that for PMo/ZIF-67-6-6N, implying the lower content of Co^0 in former than later. The combination of XRD and XPS indicates the removement of most of Co NPs from PMo/ZIF-67-6-6N by acid etching.

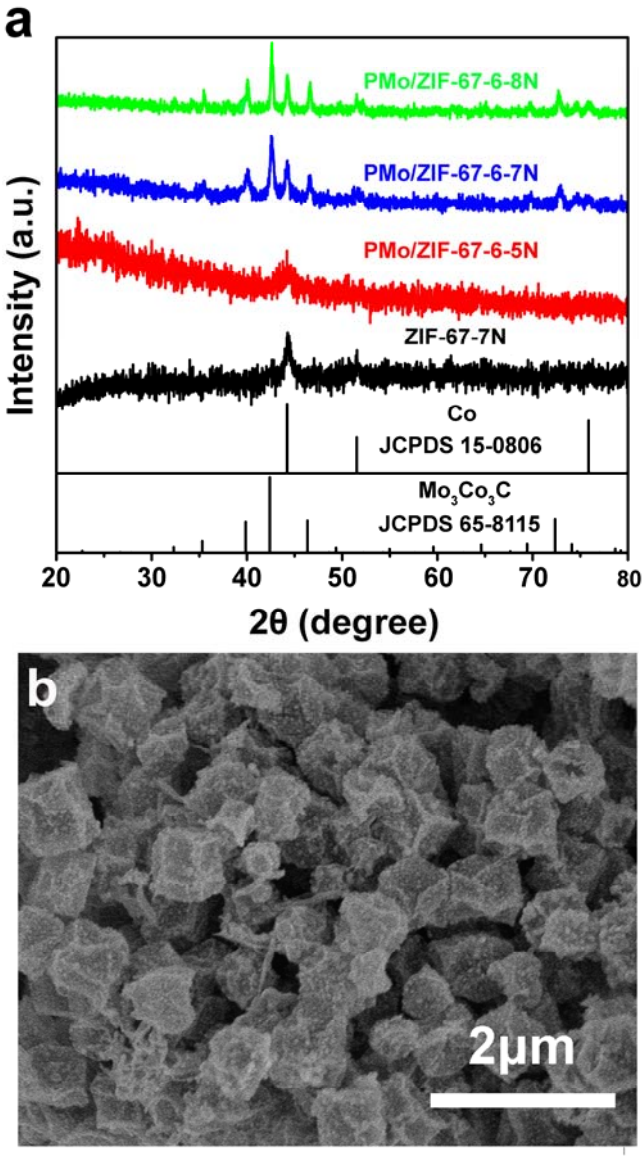

Figure S14. (a) XRD patterns of PMo/ZIF-67-6-5N, PMo/ZIF-67-6-7N, PMo/ZIF-67-6-8N and ZIF-67-7N; (b) the SEM image of PMo/ZIF-67-6-7N.

Figure S14a shows XRD patterns of PMo/ZIF-67-6-5N, PMo/ZIF-67-6-7N, PMo/ZIF-67-6-8N and ZIF-67-7N. We can observe Co peaks for PMo/ZIF-67-6-5N from calcinating PMo/ZIF-6 at 500°C, and there are no obvious peaks relative with carbides. The sample from the calcination of PMo/ZIF-67-6 at 600 °C is composed of Mo_6Co_6C with little amount of Co metal (Figure S5, 6). When increasing the calcination temperature to 700°C, the intensive peaks corresponding to Co_3Mo_3C can be seen, in company with little amount of Co. No peaks about mono-metal carbides can be observed, such as cobalt carbide and molybdenum carbide in PMo/ZIF-67-6-7N. The PMo/ZIF-67-6-8N shows similar XRD pattern with

PMo/ZIF-67-6-7N, but with more marrow peaks due to the formation of large particles induced by high temperature. In addition, only peak of metal Co can be observed for the sample of ZIF-67-7N. The results indicate that 1) the higher temperature are favourable to the formation of the bi-metal carbide, and 2) the components and size of materials can be tuned by changing the synthetic parameters. The SEM image of PMo/ZIF-67-6-7N shows the presence of polyhedrons with relative uniform size and morphology. There are many partices on polyhedrons, ascribing to the formation of BTMCs. The particle sizes are larger than that on PMo/ZIF-67-6-6N polyhedrons due to high calcination temperature.

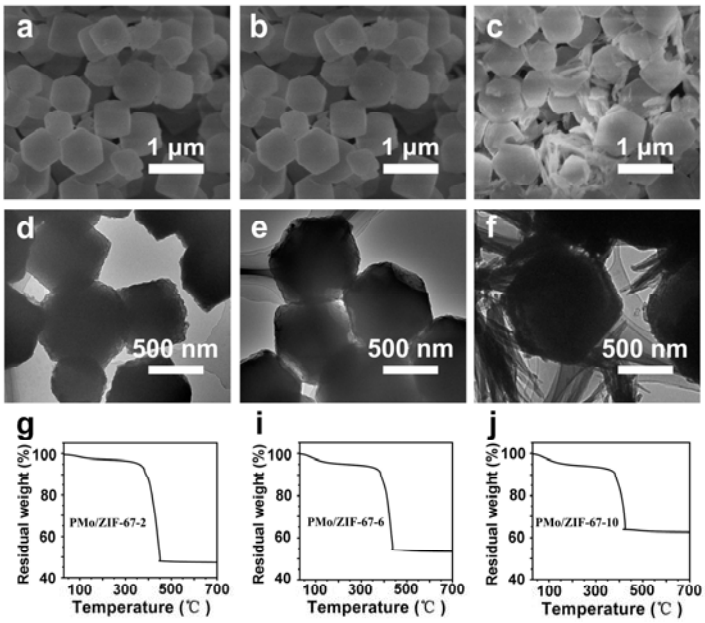

Figure S15. SEM images of (a) PMo/ZIF-67-2, (b) PMo/ZIF-67-6 and (c) PMo/ZIF-67-10. The TEM images of d) PMo/ZIF-67-2, (e) PMo/ZIF-67-6 and (f) PMo/ZIF-67-10. The g-j is the TG curves of PMo/ZIF-67-2, PMo/ZIF-67-6 and PMo/ZIF-67-10 under air atmosphere.

Figure S15 shows SEM images of PMo/ZIF-67-2, PMo/ZIF-67-6 and PMo/ZIF-67-10. It is obvious that the presence of regular polyhedrons in PMo/ZIF-67-2 (a, d), PMo/ZIF-67-6 samples (b, e). While for PMo/ZIF-67-10, there are presence of the particles with non-polyhedron morphology besides regular polyhedrons. The result indicates that catching too much of PMo_{12} can result in the damage of the structure of ZIF-67, just like that the excessive gas can make the balloon explosion. Thus, the control of the trapping time is very important to obtain

PMo/ZIF-67-x with regular morphology of ZIF-67.

Figure S15 g-j gives TG curves of PMo/ZIF-67-2, PMo/ZIF-67-6 and PMo/ZIF-67-10 under air atmosphere. It is shown that the loss weight is about 53% for PMo/ZIF-67-2 in the range of 30 to 700 °C. Under the same temperature range, the mass lose of PMo/ZIF-67-6 and PMo/ZIF-67-10 are about 47% and 37.5% of its initial mass respectively. We can see that the mass loss is decreased in order of PMo/ZIF-67-2 > PMo/ZIF-67-6 > PMo/ZIF-67-10. The little loss weight implies the high amount of PMo_{12} in PMo/ZIF-67 samples. The result indicates the that the amount of PMo_{12} in final solid increase with the increase of the solve-thermal time.

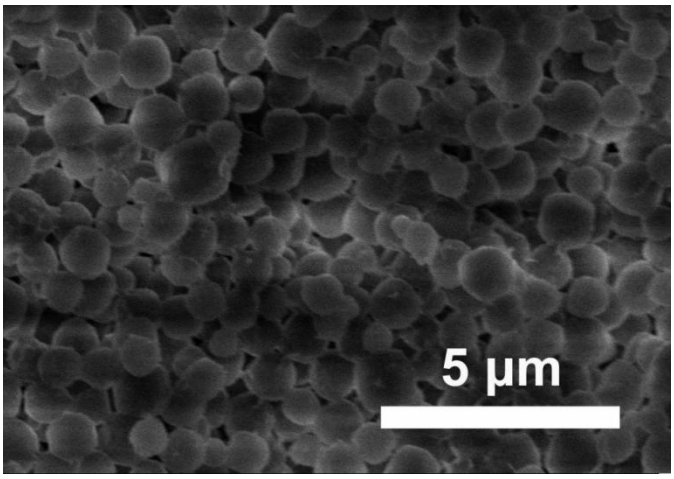

Figure S16. SEM image of Na_2MoO_4/ZIF-67-6 prepared with Na_2MoO_4 as Mo source.

Figure S16 shows SEM image of Na_2MoO_4/ZIF-67-6 prepared with Na_2MoO_4 as Mo source. We can see the presence of many irregular particles, implying the damage of the morphology of ZIF-67 in this case.

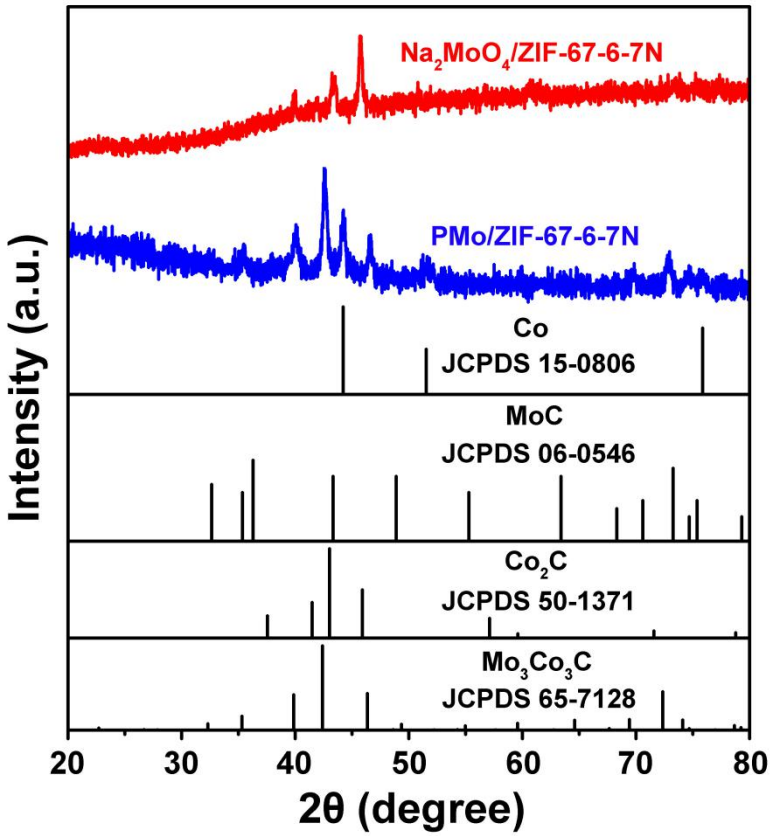

Figure S17. XRD patterns of PMo/ZIF-67-6-7N and Na_2MoO_4/ZIF-67-6-7N prepared in the presence of $H_3PMo_{12}O_{40}$ and $Na_2MoO_4 \cdot 2H_2O$ as Mo source, respectively.

We further studied the impact of the differrent kinds Mo source on the final products. To this, the $H_3PMo_{12}O_{40}$ was instead by $Na_2MoO_4 \cdot 2H_2O$ in the solvothermal process to obtain Na_2MoO_4/ZIF-67-6. After calcination under N_2, Na_2MoO_4/ZIF-67-6-7N was obtained. Figure S14 shows the XRD patterns of PMo/ZIF-67-6-7N and Na_2MoO_4/ZIF-67-6-7N. It is worth noting that Mo_6Co_6C (JCPDS 65-8115) can be obtained in the case of using PMo_{12} as Mo source (PMo/ZIF-67-6-7N). For Na_2MoO_4/ZIF-67-6-7N which obtained from the use of Na_2MoO_4 as Mo source, a mixture of MoC (JCPDS 06-0546) and Co_2C (JCPDS 50-1371) can be formed. The formation of mixture is relative to the weak interaction of $Na_2MoO_4 \cdot 2H_2O$ with 2-MIM and small molecular size, which is not favorable for the stabilization of Mo source in cage and their contact with Co source in close distance.

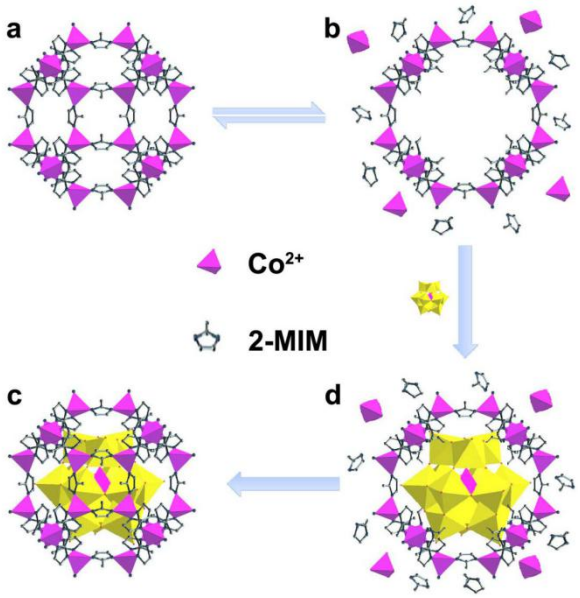

Scheme S1. The formation mechanism of PMo/ZIF-67.

When ZIF-67 was heated in methanol, partial of 2-MIM and Co^{2+} of ZIF-67 dissolved in the solvent. The disassembly process can make the formation of some defects, thus opening the window of ZIF-67 and allowing the access of PMo_{12} into ZIF-67 cage. The cage can accommodate PMo_{12} after opening the window due to the suitable size. Also, the residual 2-MIM in cages can coordinate with PMo_{12}, making the stabilization of PMo_{12} in cages. The reassembly of Co^{2+} and 2-MIM on ZIF-67 (especially under cooling process) and the coordination between PMo_{12} and residual 2-MIM in cages can make the stabilization and encapsulation of PMo_{12} in cages. The flexibility of the trapping process makes easy tune of the trapping amount of PMo_{12} in ZIF-67 by tuning reaction time. The amount of PMo_{12} in final PMo/ZIF-67 increase with the increase of solve-thermal time. Also, the trapping of too much PMo_{12} can result in the damage of the structure of ZIF-67, just like the blast of balloon as filling too much gases.

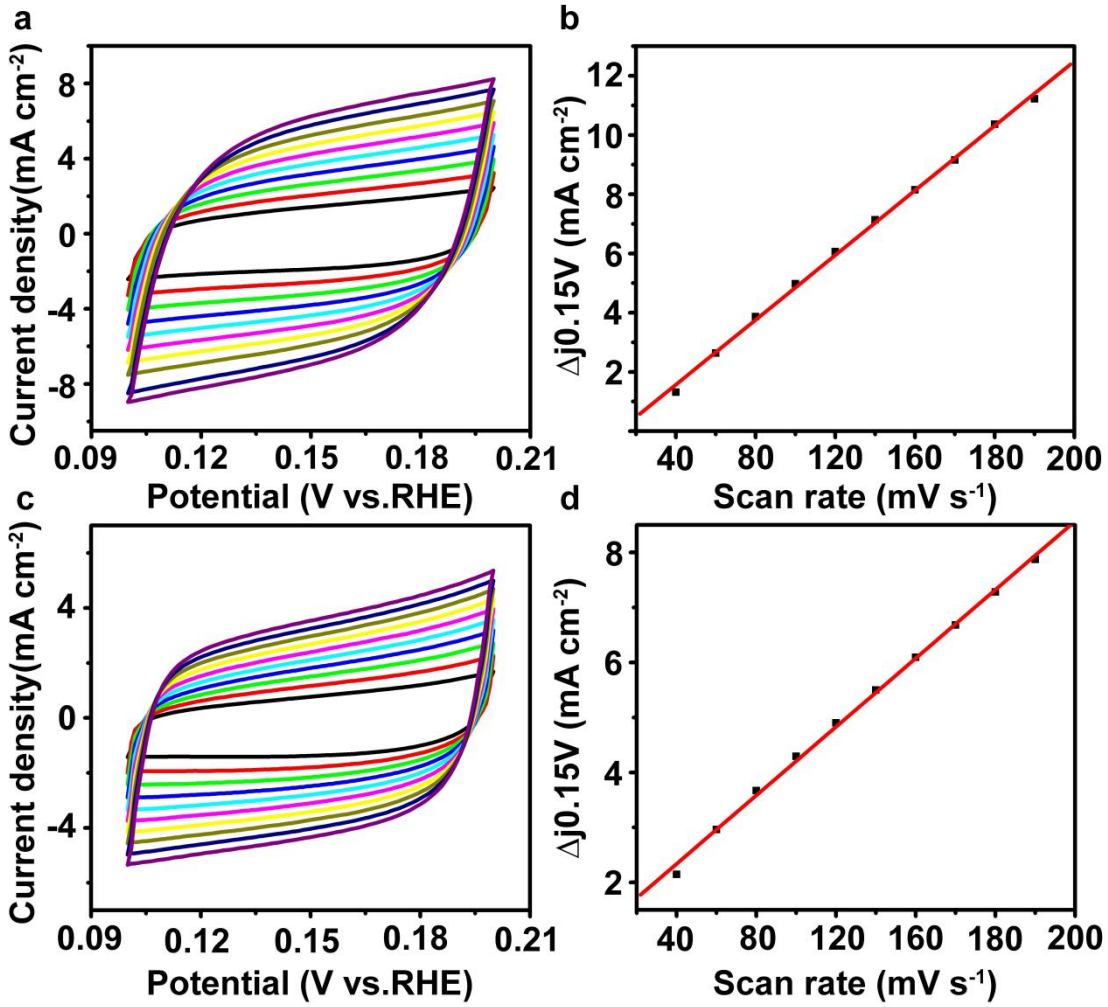

Figure S18. Cyclic voltammograms (CV) of PMo/ZIF-67-6-6N (a) and ZIF-67-6N (c) taken under different rates from 40 to 220 mVs^{-1}. The corresponding capacitive current at 0.15 V as a function of scan rate for PMo/ZIF-67-6-6N (b) and ZIF-67-6N (d).

In order to evaluate the electrochemical active surface areas, the cyclic voltammetry (CV) method was used to measured the electrochemical double layer capacitance (EDLC, Cdll) of the studied catalysts. The Cdll values of PMo/ZIF-6-6N is 27.32 mF cm^{-2}, much higher than that of ZIF-67-6N (15.58 mF cm^{-2}),which is associated with its large exchange current density (0.67mA cm^{-2}).

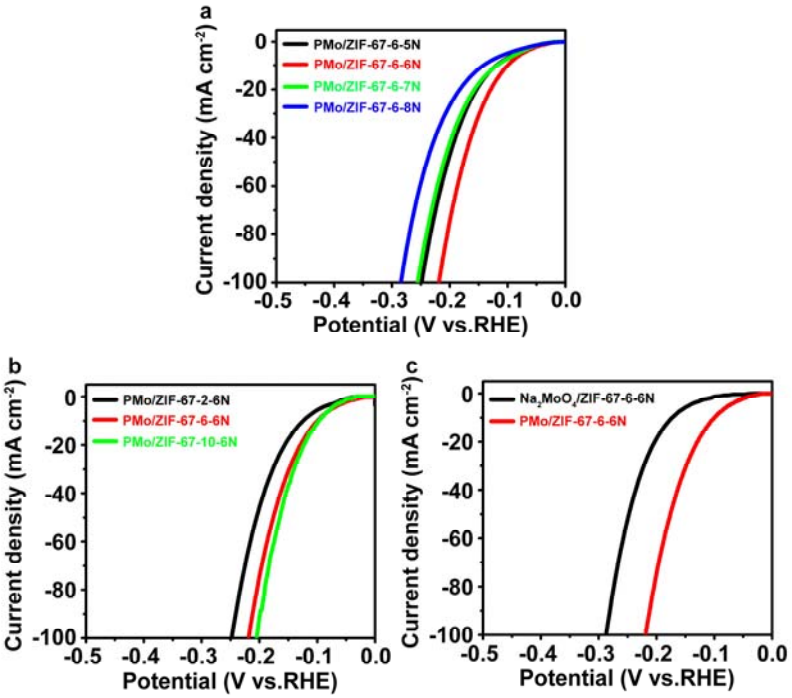

Figure S19. (a) Polarization curves of the PMo/ZIF-67-6 calcinated at 500, 600, 700 and 800℃under N_2 in 1M KOH at the scan rate of 5 mVs^{-1} for HER. (b) Polarization curves of PMo/ZIF-67-2-6N, PMo/ZIF-67-6-6N and PMo/ZIF-67-10-6N in 1M KOH at the scan rate of 5 mVs^{-1} for HER. (c) Polarization curves of Na_2MoO_4/ZIF-67-6-6N and PMo/ZIF-67-6-6N under the same condition for HER.

We calcinate PMo/ZIF-67-6 at different temperature and find that the catalyst treated at 600℃shows the best HER performance (Figure S19 a). When we adjust the the solvothermal time of the precursor, we can acknowledge that there is little difference between PMo/ZIF-67-6-6N and PMo/ZIF-67-10-6N (Figure S19 b). But the morphology for PMo/ZIF-67-6-6N is much more regular. We also use $Na_2MoO_4 \cdot 2H_2O$ as Mo source instead of $H_3PMo_{12}O_{40}$, the obtained material displays poorer HER catalytic activities than the catalyst prepared with $H_3PMo_{12}O_{40}$ (Figure S19 c).

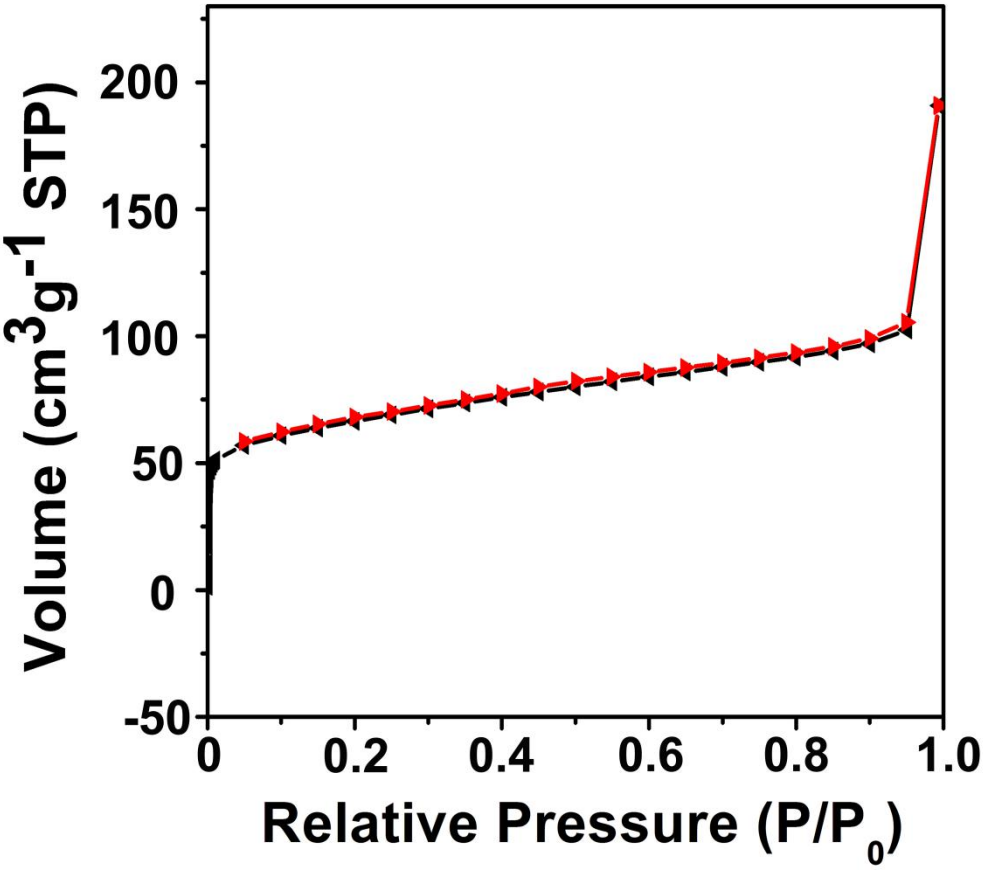

Figure S20. N_2 adsorption-desorption isotherms of PMo/ZIF-67-6-6N.

The N_2 adsorption-desorption isotherms of PMo/ZIF-67-6-6N revealed that the sample has Type I isotherm. The Brunauer−Emmett−Teller (BET) surface area of PMo/ZIF-67-6-6N is about 240 m^2/g.

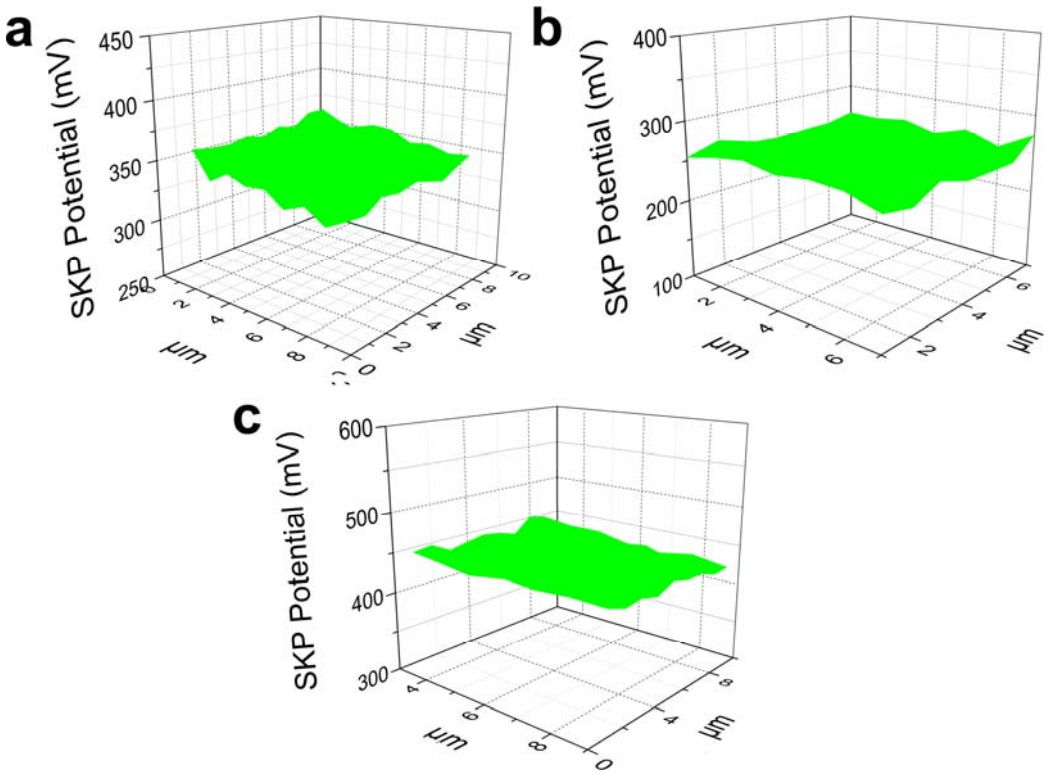

Figure S21. Work function (WF) drawings of (a) PMo/ZIF-67-6-6N and (b) Pt/C and (c) ZIF-67-6N.

The surface work function (WF) represents the ability of catalysts to trap electrons, which is measured by scanning kelvin probe test (SKP). The Scanning Kelvin Probe (SKP) technique is a non-destructive test method that can detect differences across the surface of a sample. The high WF value of Pt leads to it's remarkable performance for HER. The PMo/ZIF-67-6-6N shows work function (WF) of 5.68 eV (Figure S20a). The WF of ZIF-67-6N is about 5.78 eV (Figure S20c). The PMo/ZIF-67-6-6N give work function more close to Pt (Figure S20b), implies the enhanced trapping ability to electrons after surface activation.

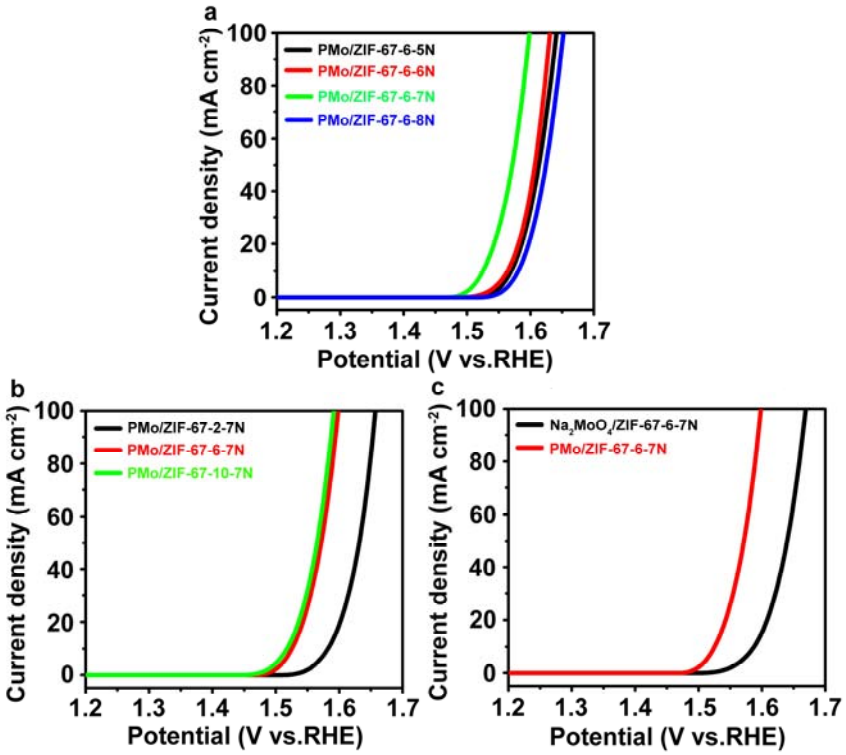

Figure S22. (a) Polarization curves of PMo/ZIF-67-6 calcinated at 500, 600, 700 and 800℃under N_2 in 1M KOH at the scan rate of 5 mVs^{-1} for OER. (b) Polarization curves of PMo/ZIF-67-2-7N, PMo/ZIF-67-6-7N and PMo/ZIF-67-10-7N in 1M KOH at the scan rate of 5 mVs^{-1} for OER. (c) Polarization curves of Na_2MoO_4/ZIF-67-6-7N and PMo/ZIF-67-6-7N under the same condition for OER.

From Figure S22, we can see that PMo/ZIF-67-7N exhibits highest activity for OER than the catalysts obtained from other preparation conditions. At the same time, the catalyst prepared by using PMo_{12} as Mo source shows better activity than that prepared by using Na_2MoO_4 as Mo source for OER. Above results indicate the important effect of the synthetic parameters on the performance.

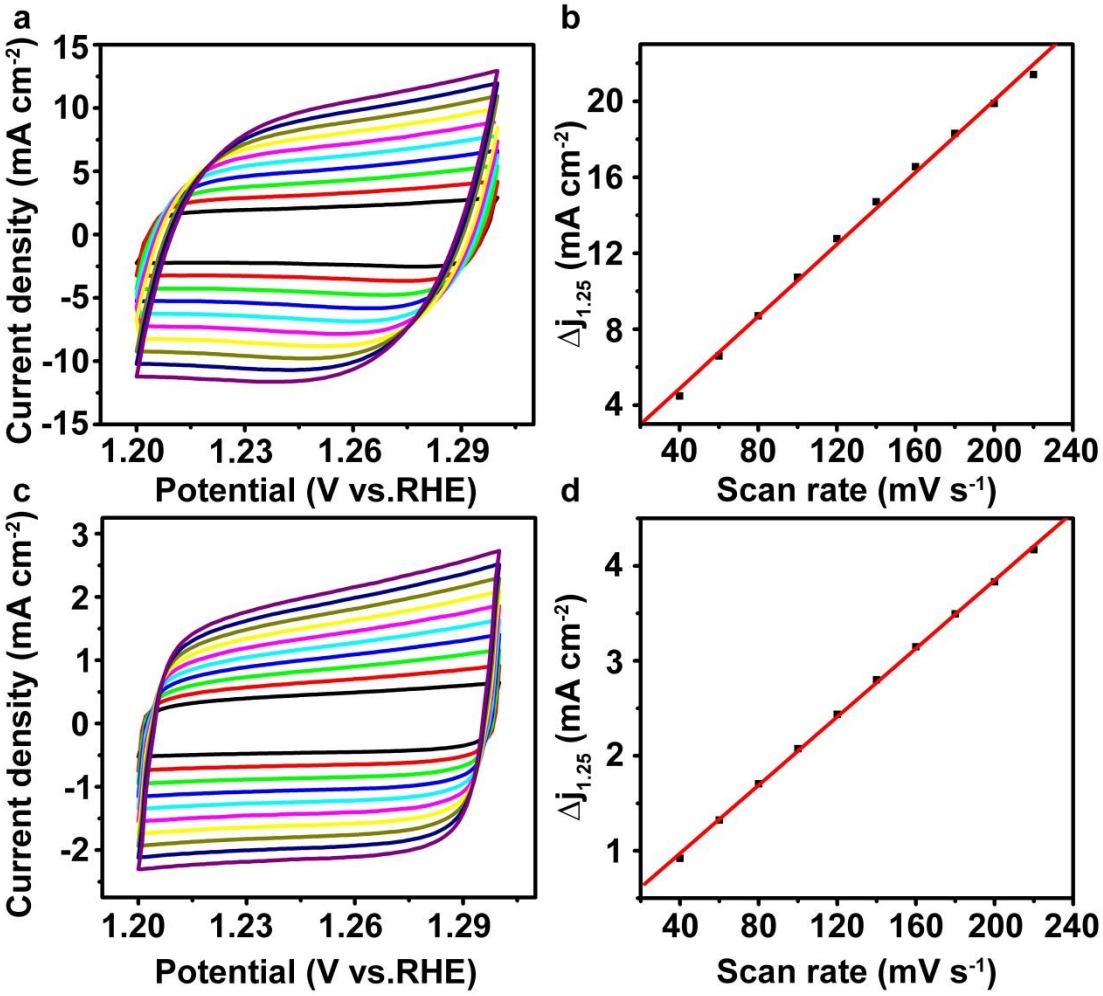

Figure S23. Cyclic voltammograms (CV) of (a) PMo/ZIF-67-6-7N and (c) ZIF-67-7N taken under different rates from 40 to 220 mVs^{-1}. The corresponding capacitive currents at 1.25 V as a function of scan rate for (b) PMo/ZIF-67-6-7N and (d) ZIF-67-7N.

The cyclic voltammetry (CV) method was used to study details on charge storage capabilities of the electrocatalysts, which can be used to evaluate the electrochemical active surface areas of the catalysts. The Cdl values of PMo/ZIF-67-6-7N and ZIF-67-7N are 47.4 and 9.0 mF cm^{-2}, respectively. It is obviously that PMo/ZIF-67-6-7N has a much higher electrochemically active surface area than ZIF-67-7N.

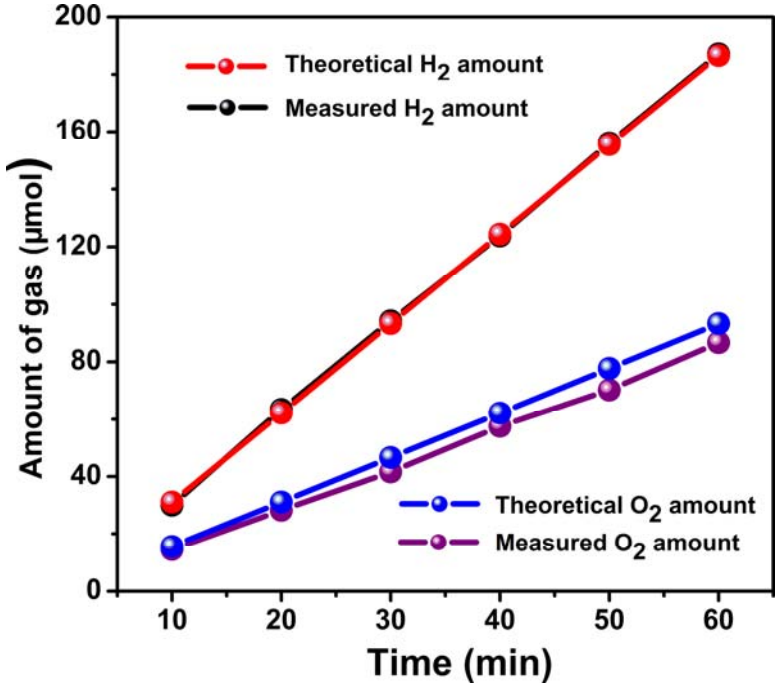

Figure S24. The experimentally determined and theoretically calculated amounts of H_2 on PMo/ZIF-67-6-6N and O_2 on PMo/ZIF-67-6-7N. The Faradic efficiency (FE) is close to 100% for HER and 93% for OER at test of 60 min.

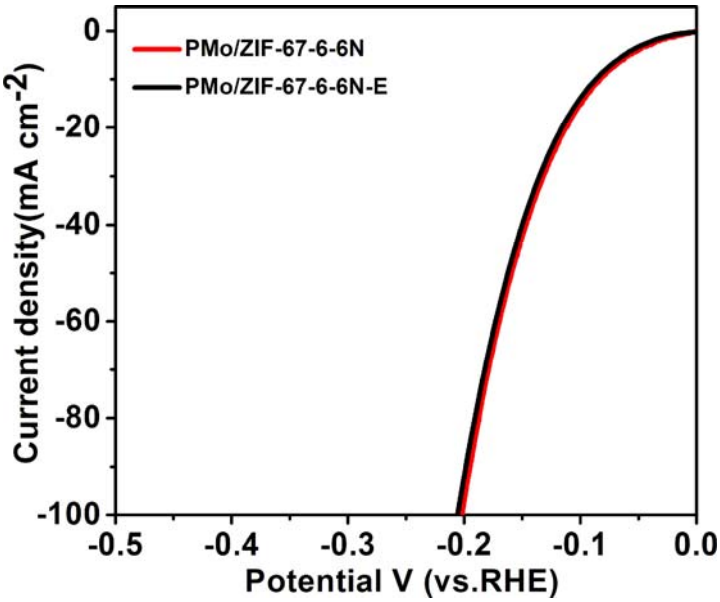

Figure S25. HER performance of PMo/ZIF-67-6-6N and PMo/ZIF-67-6-6N-E (E represented etching) in 1M KOH. The performance have no obvious change before and after etching of Co NPs.

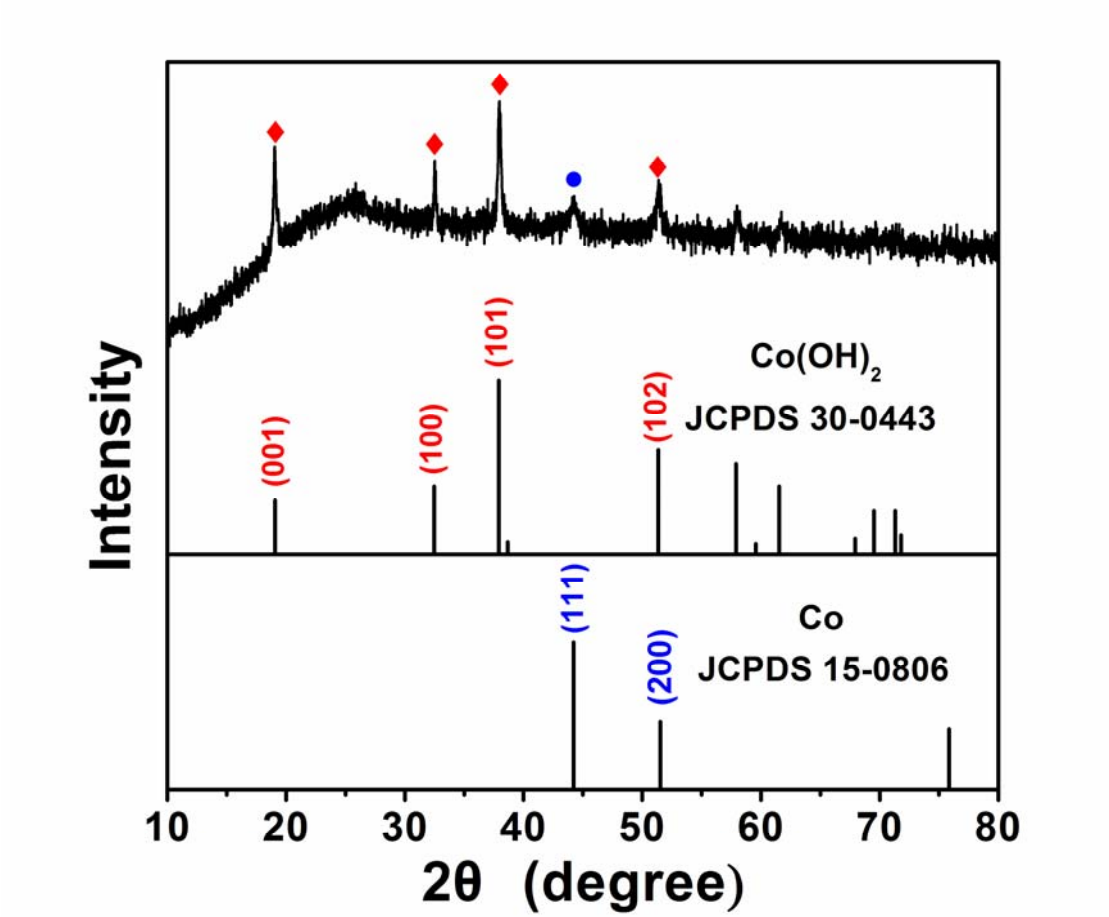

Figure S26. XRD pattern of PMo/ZIF-67-6-7N after OER test (40 CV cycles).

Figure S26 shows XRD pattern of PMo/ZIF-67-6-7N after OER test (40 CV cycles). The XRD patterns show the existence of intensive peaks of CoOH in company with the slight low peaks of Co metal, indicating the oxidation of Co in PMo/ZIF-67-6-7N. The peaks of carbides can not be obviously seen.

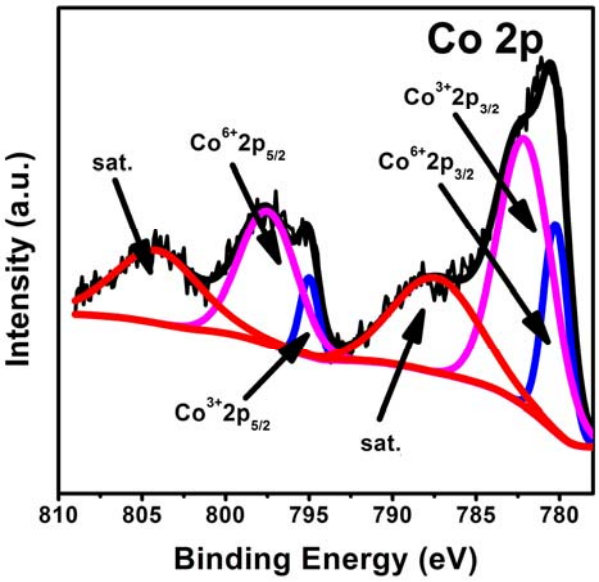

Figure S27. XPS of Co2p of PMo/ZIF-67-6-7N after OER test (40 CV cycles).

The high-resolution Co 2p spectrum can be deconvoluted into six peaks. The two peaks at 780.2 and 795.0 eV corresponding to the $2p_{3/2}$ and $2p_{5/2}$ of Co^{3+}. The peaks related to Co^{2+} $2p_{3/2}$ and $2p_{5/2}$ are located at 782.1 and 797.5eV. The XPS of Co^{2+} and Co^{3+} can be ascribed to $Co(OH)_2$, being consistent with XRD result.

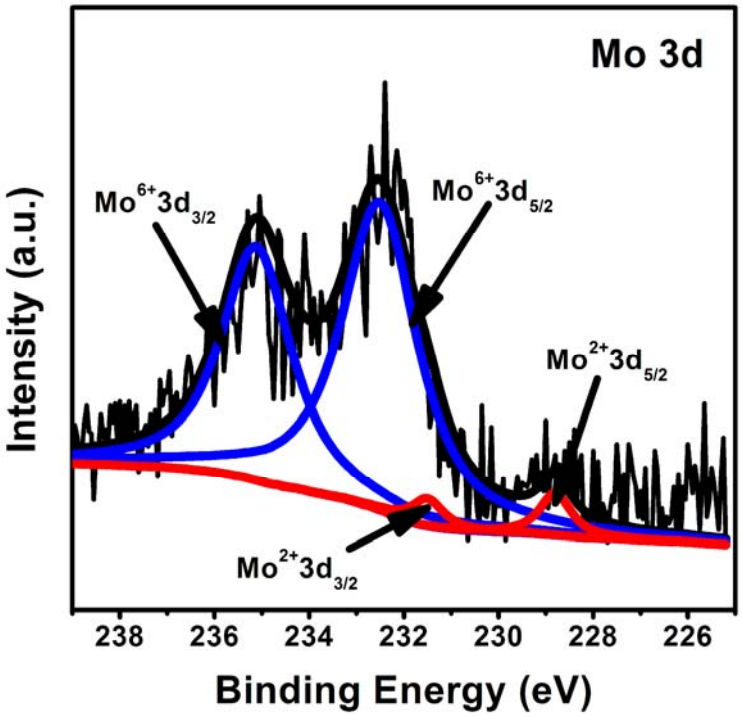

Figure S28. XPS of Mo3d of PMo/ZIF-67-6-7N after OER test (40 CV cycles).

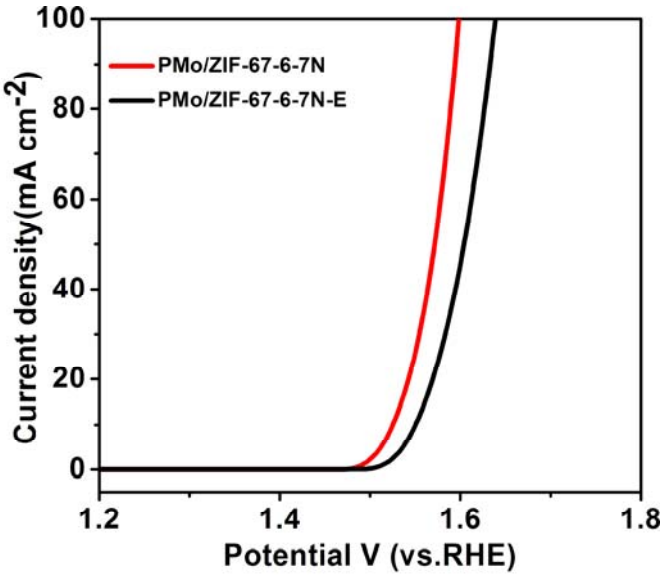

Figure S29. The OER performance of PMo/ZIF-67-6-7N and PMo/ZIF-67-6-7N-E (E represented etching of Co NPs in H_2SO_4) in 1M KOH. The η10 and η100 for PMo/ZIF-67-6-7N are 295 and 370mV respectively, lower than 320 and 410mV for PMo/ZIF-67-6-7N-E. The result indicate the contribution of Co NPs in PMo/ZIF-67-6-7N on OER.

Figure S30. The photograph for overall water splitting reaction in a two-electrode configuration. The inset is an optical photograph showing the generation of H_2 and O_2 bubbles for PMo/ZIF-67-6-6N||PMo/ZIF-67-6-7N on Ni foam.

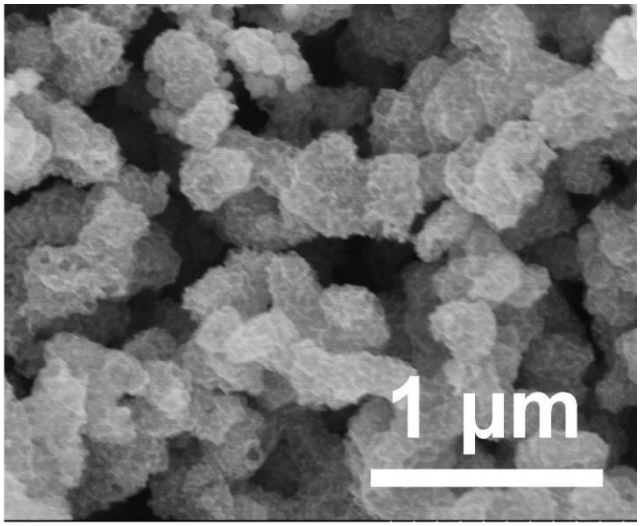

Figure S31. SEM image of S-PMo/ZIF-67-6N.

Figure S31 shows SEM image of S-PMo/ZIF-67-6N. We can observe the formation of spheres with crumpled surface. The morphology is obviously different from the regular polyhedron morphology of PMo/ZIF-67-6-6N.

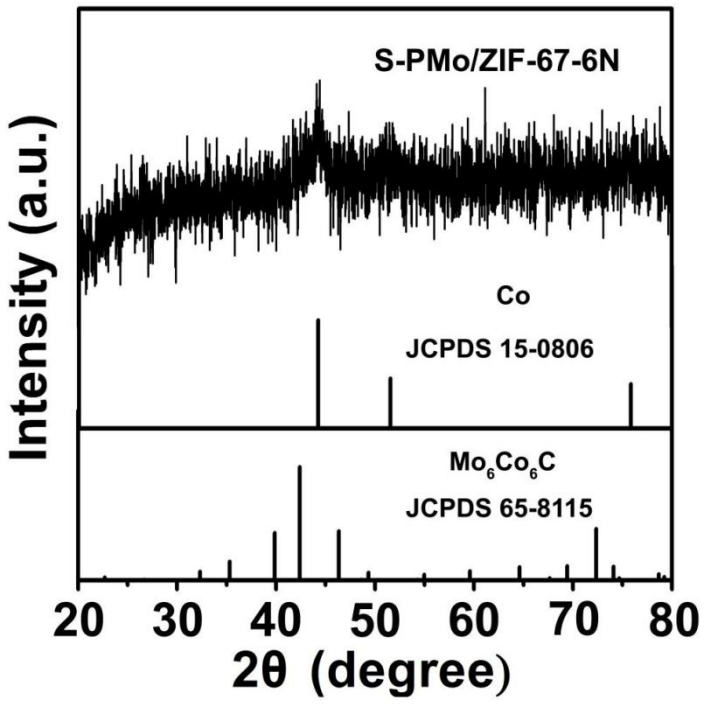

Figure S32. XRD patterns of S-PMo/ZIF-67-6N.

The XRD patterns of sample (S-PMo/ZIF-67-6N) prepared based on simultaneous route (like POMOF-based route) is mainly composed of Co with no obvious peaks corresponding to Mo_XCo_XC. In contrast, the sample (PMo/ZIF-67-6-6N) obtained based on "trapping" route is composed of Mo_6Co_6C and Co. It is obvious that the "trapping" route is effective to give Mo_XCo_XC.

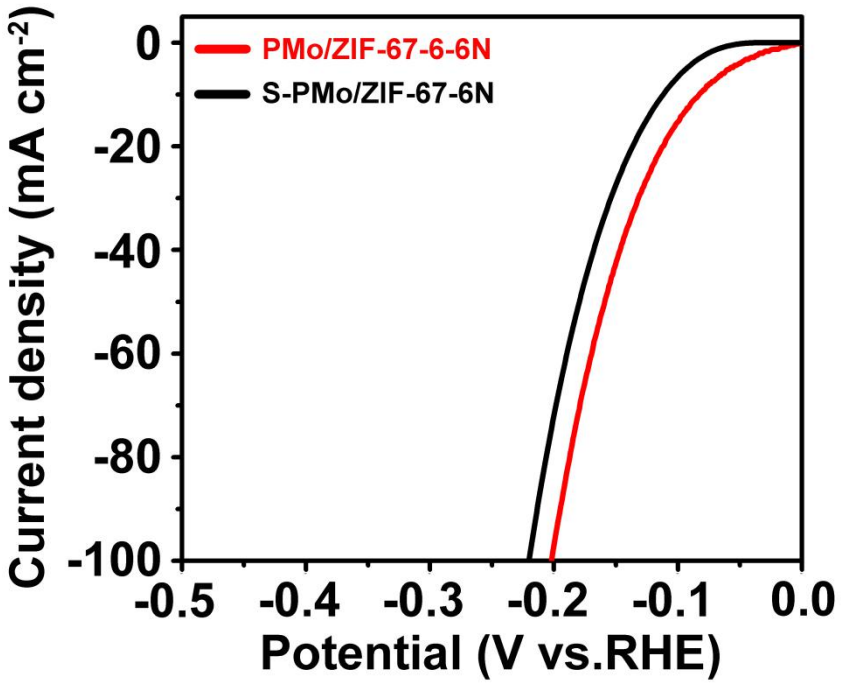

Figure S33. Polarization curves of PMo/ZIF-67-6-6N and S-PMo/ZIF-67-6N in 1M KOH at the scan rate of 5 mVs^{-1} for HER.

Figure S33 shows the polarization curves of PMo/ZIF-67-6-6N and S-PMo/ZIF-67-6N in 1M KOH at the scan rate of 5 mVs^{-1} for HER. In order to reach the current density of 10 mA cm^{-2}, S-PMo/ZIF-67-6N needs an overpotential of 114 mV, whereas PMo/ZIF-67-6-6N only requires an overpotential of 83 mV. Thus, the catalyst prepared based on "trapping" route exhibits better activity than that of the catalyst obtained based on simultaneous route (like POMOF-based route) for HER.

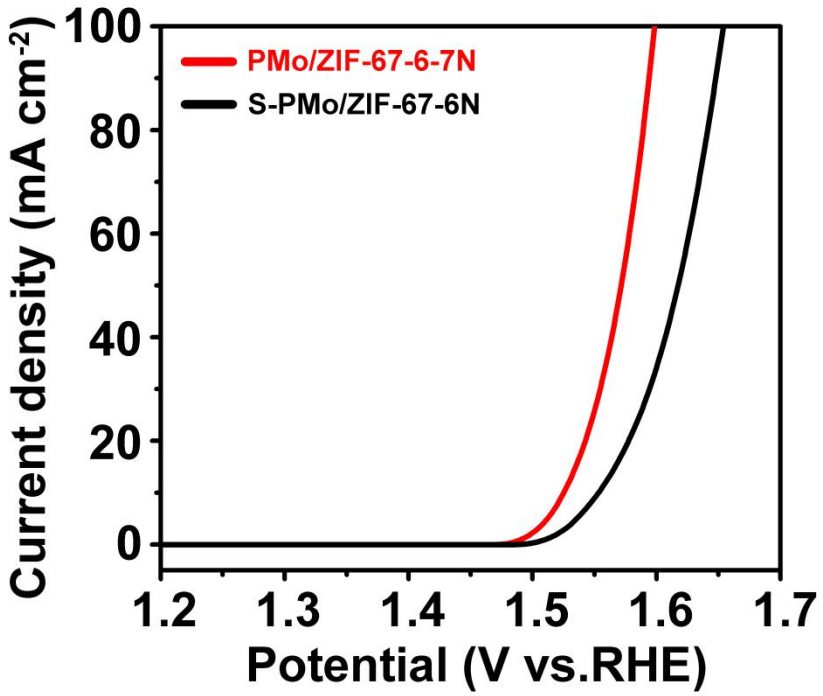

Figure S34. Polarization curves of PMo/ZIF-67-6-7N and S-PMo/ZIF-67-6N in 1M KOH at the scan rate of 5 mVs^{-1} for OER.

Figure S34 shows the polarization curves of PMo/ZIF-67-6-7N and S-PMo/ZIF-67-6N in 1M KOH at the scan rate of 5 mVs^{-1} for OER. As for PMo/ZIF-67-6-7N, an overpotential of 295 mV is needed to reach the current density of 10 mA cm^{-2}, while S-PMo/ZIF-67-6N needs the overpotential of 330 mV. In addition, the overpotential of 430mV and 370mV are needed to reach the current density of 100 mA cm^{-2} for S-PMo/ZIF-67-6N and PMo/ZIF-67-6-7N respectively. It is obviously that PMo/ZIF-67-6-7N prepared based on "trapping" route shows superior performance for OER to the catalyst obtained based on simultaneous route.

Table S2. Comparison of HER performance of PMo/ZIF-67-6-6N with other non-noble metal HER electrocatalysts in alkaline condition.

Catalyst	Loading density (mg/cm^2)	Current density (j) ($mA\ cm^{-2}$)	Overpotential at corresponding J (mV)	IR compensation	Reference
Mo_2C micro-particles	0.8	10	190	√	*Angew. Chem. Int. Ed*. **2012**, *51*, 12703.
Bulk MoB	2.3	1	150		
Mo_2C Nanotube	0.75	10	112	√	*Angew. Chem. Int. Ed*. **2015**, *54*, 15395
MoxC	——	10	128	√	*Nanoscale,* **2017**,9, 7260–7267
Mo_2C nanorods	0.43	10	130	√	*Appl. Catal. B: Environ.,* **2014**, *154*, 232-237.
MoP/FTO	0.1	10	190	√	*J.Mater. Chem.A,* **2015**,*3*, 4368–4373
Mo_2C@NC	~0.28	10	60	√	*Angew.Chem.Int.Ed*. **2015,***54*, 10752 –10757
Mo_2C	0.102	10	176	——	*J. Mater. Chem. A* **2015**, *3*, 8361.
Mo_2N			353		
MoP	0.86	10	150	——	*Energy Environ. Sci.* **2014**,*7*, 2624
MoC/C	——	10	138	——	*J.Mater. Chem.A,* **2017**,*5*, 4879–4885
Mo_2C/C			96		
MoCx	0.8	10	151	——	*Nat. Commun.,* **2015**,*6*, 6512-6519.
Mo_2C-C	0.84	10	149	——	*Nano Energy* **2017**,*32 511–519*
MoP-C		10	169		
MoS_2-C		10	203		
MoS_2@MoP	0.35	10	119	——	*Nanoscale,* **2016**,*8*, 11052–11059
MoP	0.86	10	~140	——	*Energy Environ. Sci.,* **2014**,*7*, 2624–2629

MoxC-Ni@ NCV	1.1	10	126	——	*J.Am.Chem. Soc.***2015**, *137*, 15753 - 15759
Mo_2C embedded N-doped carbon nanotubes	~ 3	10	257	——	*J.Mater. Chem. A*, **2015**,*3*, 5783
Co-P film	——	10	94	√	*Angew. Chem.Int. Ed.***2015**, *54*, 6251 –6254
CoP/CC	0.92	10	209	——	*J.Am.Chem. Soc*.**2014**, *136*, 7587−7590
Co-NRCN Ts	0.28	1	160	——	*Angew. Chem., Int. Ed.* **2014**, *53*,4372
		10	370		
Co-P/NC	0.283	10	191	——	*Chem. Mater.* **2015**, *27*, 7636−7642
		20	212		
		100	277		
	1.0	10	154		
		20	173		
		100	234		
CoMoS	0.84	10	98	.——	ACS Appl. Mater. Interfaces 2017, 9, 5288−5294
PMo/ZIF-67-6-6N	0.708	10	83	√	This work

Table S3. The HER performance of catalysts from the calcination of PMo/ZIF-67-6 at different temperature.

Catalyst	**onset overpotential (mV)**	**η_{10} (mV)**	**η_{100} (mV)**
PMo/ZIF-67-6-5N	69	119	249
PMo/ZIF-67-6-6N	36	83	202
PMo/ZIF-67-6-7N	69	118	256
PMo/ZIF-67-6-8N	109	142	284

Table S4. The HER performance of catalysts prepared by the calcination of PMo/ZIF-67 from different solvothermal time.

Catalyst	**onset overpotential (mV)**	**η_{10} (mV)**	**η_{100} (mV)**
PMo/ZIF-67-2-6N	53	125	248
PMo/ZIF-67-6-6N	36	83	202
PMo/ZIF-67-10-6N	35	83	190

Table S5. The HER performance of catalysts from the calcination of the precursor prepared by using Na_2MoO_4 and PMo_{12} as Mo source.

Catalyst	**onset overpotential (mV)**	**η_{10} (mV)**	**η_{100} (mV)**
Na_2MoO_4/ZIF-67-6-6N	102	173	287
PMo/ZIF-67-6-6N	36	83	202

Table S6. The HER performance of catalysts prepared based on "tapping" route and "simultaneous" route (POMOF-based route).

Catalyst	**onset overpotential (mV)**	**η_{10} (mV)**	**η_{100} (mV)**
S-PMo/ZIF-67-6N	71	114	221
PMo/ZIF-67-6-7N	36	83	202

Table S7. The OER performance of catalysts from the calcination of PMo/ZIF-67-6 at different temperature.

Catalyst	**onset overpotential (mV)**	**η_{10} (mV)**	**η_{100} (mV)**
PMo/ZIF-67-6-5N	330	340	410
PMo/ZIF-67-6-6N	320	330	400
PMo/ZIF-67-6-7N	280	295	370
PMo/ZIF-67-6-8N	340	350	420

Table S8. The OER performance of catalysts prepared by the calcination of PMo/ZIF-67 from different solvothermal time**.**

Catalyst	**onset overpotential (mV)**	**η_{10} (mV)**	**η_{100} (mV)**
PMo/ZIF-67-2-7N	270	350	420
PMo/ZIF-67-6-7N	280	295	370
PMo/ZIF-67-10-7N	340	290	360

Table S9. The OER performance of catalysts from the calcination of the precursor prepared by using Na_2MoO_4 and PMo_{12} as Mo source.

Catalyst	**onset overpotential (mV)**	**η_{10} (mV)**	**η_{100} (mV)**
Na_2MoO_4/ZIF-67-6-7N	330	360	440
PMo/ZIF-67-6-7N	280	295	370

Table S10. The OER performance of catalysts prepared based on "tapping" route and "simultaneous" route (POMOF-based route).

Catalyst	**onset overpotential (mV)**	**η_{10} (mV)**	**η_{100} (mV)**
S-PMo/ZIF-67-6N	280	330	430
PMo/ZIF-67-6-7N	280	295	370

Table S11. Comparison of OER performance of PMo/ZIF-67-6-7N with other non-noble metal OER electrocatalysts in alkaline conditions.

Catalyst	Loading density (mg/cm^2)	Current density (j) ($mA\ cm^{-2}$)	Overpotential at corresponding j (mV)	IR compensation	Reference
NiFe-PVP	——	10	297	√	Adv. Energy Mater. **2017**, 1700220
Ni–Mo nitride	3.5	10	295	√	J. Mater. Chem. A, **2017**, 13648
$MoNi_4$/Ni foam	~1.09	10	280	√	J.Mater.Chem.A, **2017**, 5, 2508
MoS_2/Ni_3S_2/ Ni foam	9.7	10	218	——	Angew.Chem. Int. Ed., **2016**, 128, 6814
Co-P film	——	10	345	√	Angew. Chem. Int. Ed., **2015**, 127, 6349
NiCoP	~1.6	10	280	√	Nano Lett., **2016**, 16, 7718
$NiCo_2S_4$NW/ NF	——	10	260	√	Adv. Funct. Mater. 2016, 26, 4661–4672
CP/CTs/Co-S	~0.32	10	306	√	ACS Nano 2016, 10, 2342
$NiCo_2O_4$	~1	10	290	√	Angew. Chem. Int. Ed. 2016, 55, 6290
CoP	3.3	10	281	√	ChemSusChem 2016, 9, 472 – 477
CoP	~0.05	10	360	√	ACS Catal. 2015, 5, 4066

PCPTF	0.1	30	330	√	Adv Mater 2015, 27, 3175
$NiCo_2S_4$	4	10	280	√	Nanoscale 2015, 7, 15122
$CoFe_2O_4$	~1.031	10	378	——	Acs Appl Mater Inter 2015, 7, 17851.
Co_9S_8	5	10	320	——	Adv. Funct. Mater. **2017**, 1606585
Co/CoP	——	10	345	——	Angew Chem Int Edit 2015, 54, 6251
$Co(S_xSe_{1-x})_2$	~1	10	307	——	Adv. Funct. Mater. **2017**, 1701008
PMo/ZIF-67-6-7N	0.708	10	295	√	This work

Table S12. The performance of the recent reported electrocatalysts in alkaline solution for overall water splitting.

Catalyst	Overpotential at 10 mA cm^{-2} (mV)		Tafel slope ($mV\ dec^{-1}$)		Overall water voltage at 10 mA cm^{-2}(V)	Reference
	HER	OER	HER	OER		
MoS_2/Ni_3S_2/ Ni foam	110	218	83	88	1.56	Angew.Chem. Int. Ed., **2016**, 128, 6814
NiMo-PVP/ NiFe-PVP	130	297	84	48	1.66	Adv. Energy Mater. **2017**, 1700220
Ni–Mo nitride	89	295	79	94	1.60	J. Mater. Chem. A, **2017**, 13648
$MoNi_4$/Ni foam	28	280	36	79	1.58	J. Mater. Chem. A, **2017**, 5, 2508
Co_9S_8	340	320	68	105	1.60	Adv. Funct. Mater. **2017**, 1606585
Co-P film	94	345	42	47	~1.64	Angew. Chem. Int. Ed., **2015**, 127, 6349
NiCoP	32	280	37	87	1.58	Nano Lett., **2016**, 16, 7718
$Co(S_xSe_{1-x})_2$	122	307	85.7	67.5	1.63	Adv. Funct. Mater., **2017**, 1701008
$NiCo_2S_4$ NW/NF	210	260	81.3	40.1	1.63	Adv. Funct. Mater. 2016, 26, 4661–4672

CP/CTs/Co-S	190	306	131	72	1.743	ACS Nano 2016, 10, 2342−2348
$NiCo_2O_4$	110	290	49.7	53	1.65	Angew. Chem. Int. Ed. 2016, 55, 6290 –6294
CoP	95	281	60	62	1.613	ChemSusChem 2016, 9, 472 – 477
CoP	220	360	——	83	1.81	ACS Catal 2015, 5, 4066.
Co/CoP	94	345	42	47	1.645	Angew Chem Int Edit 2015, 54, 6251
$CoxPO_4$/CoP	380	300	——	65	1.910	Adv Mater 2015, 27, 3175
$NiCo_2S_4$	263	280	141	89	1.68	Nanoscale 2015, 7, 15122
$CoFe_2O_4$	356	378	——	73	1.964	Acs Appl Mater Inter 2015, 7, 17851.
Co-CoOx/N doped Carbon	~134	260	115	——	1.624	J Am Chem Soc 2015, 137, 2688.
PMo/ZIF-67-6-7N||PMo/ZIF-67-6-6N	83	295	44.5	53	1.61	This work